

The Radcliffe Wave as traced by young open clusters*

Stellar parameters, activity indicators, and abundances of solar-type members of eight young clusters

J. Alonso-Santiago¹, A. Frasca¹, A. Bragaglia², G. Catanzaro¹, X. Fu³, G. Andreuzzi^{4,5}, L. Magrini⁶, S. Lucatello⁷, A. Vallenari⁷, and M. Jian⁸

¹ INAF–Osservatorio Astrofisico di Catania, via S. Sofia 78, 95123 Catania, Italy

² INAF–Osservatorio di Astrofisica e Scienza dello Spazio, via P. Gobetti 93/3, 40129 Bologna, Italy

³ Purple Mountain Observatory, Chinese Academy of Sciences, Nanjing 210023, China

⁴ Fundación Galileo Galilei - INAF, Rambla José Ana Fernández Pérez 7, 38712 Breña Baja, Tenerife - Spain

⁵ INAF–Osservatorio Astronomico di Roma, Via Frascati 33, 00078 Monte Porzio Catone, Italy

⁶ INAF–Osservatorio Astrofisico di Arcetri, Largo E. Fermi 5, 50125 Firenze, Italy

⁷ INAF–Osservatorio Astronomico di Padova, vicolo dell’Osservatorio 5, 35122 Padova, Italy

⁸ Department of Astronomy, Stockholm University, AlbaNova University centre, Roslagstullsbacken 21, 114 21 Stockholm, Sweden

Received / accepted

ABSTRACT

The Radcliffe Wave has only recently been recognised as a ≈ 3 kpc long coherent gas structure encompassing most of the star forming regions in the solar vicinity. Since its discovery, it has been mainly studied from the perspective of dynamics, but a detailed chemical study is necessary to understand its nature and the composition of the natal clouds that gave rise to it. In this paper we used some of the connected young open clusters (age $\lesssim 100$ Myr) as tracers of the molecular clouds. We performed high-resolution spectroscopy with GIARPS at the TNG of 53 stars that are bona fide members of seven clusters located at different positions along the Radcliffe Wave. We provide radial velocities and atmospheric parameters for all of them. For a subsample consisting of 41 FGK stars we also studied the chromospheric activity and the content of Li, from which we inferred the age of the parent clusters. These values agree with the evolutionary ages reported in the literature. For these FGK stars we determined the chemical abundances for 25 species. Pleiades, ASCC 16 and NGC 7058 exhibit a solar metallicity while Melotte 20, ASCC 19, NGC 2232, and Roslund 6 show a slightly subsolar value (≈ -0.1 dex). On average, the clusters show a chemical composition compatible with that of the Sun, especially for α - and Fe-peak elements. Neutron-capture elements, on the other hand, present a slight overabundance of about 0.2 dex, specially barium. Finally, considering also ASCC 123, studied by our group in a previous research, we infer a correlation between the chemical composition and the age or position of the clusters along the Wave, demonstrating their physical connection within an inhomogeneous mixing scenario.

Key words. stars: fundamental parameters – stars: abundances – binaries: spectroscopic – stars: activity – open clusters and associations: ASCC 16, ASCC 19, ASCC 123, Melotte 20, Pleiades, NGC 2232, NGC 7058, Roslund 6.

1. Introduction

We are currently living in a golden age for Galactic Archaeology. The ESA *Gaia* mission (Gaia Collaboration et al. 2016, 2023), in combination with other large photometric and spectroscopic surveys, is revolutionizing our knowledge of the Milky Way (for a review, see e.g. Deason & Belokurov 2024). Never before have we had at our disposal a set of astrometric, photometric and spectroscopic data of such high quality and for such a large sample of hundreds of thousands of stars. Thanks to this huge amount of information we considerably improved our understanding of the history

(see Antoja et al. 2018; Helmi et al. 2018) and components of the Galaxy. It is worth mentioning the discovery of new open clusters (OCs) and new members of already known clusters (e.g., Cantat-Gaudin et al. 2020; Castro-Ginard et al. 2020, 2022; Hunt & Reffert 2023; Cavallo et al. 2024), as well as the discovery of new associations and comoving groups in the vicinity (1–3 kpc) of the Sun (e.g., Kounkel & Covey 2019; Kounkel et al. 2020).

Recently, Alves et al. (2020) discovered a spatially coherent filamentary structure of dense gas in the solar neighbourhood when studying the 3D distribution of the local cloud complexes. This discovery was possible thanks to the accurate astrometry provided by *Gaia*, which allowed us to significantly improve the 3D mapping of the Galactic interstellar dust (Green et al. 2019; Lallement et al. 2019) and determine the distances to the local molecular clouds with great precision (Zucker et al. 2020). This structure, the so-

Send offprint requests to: J. Alonso-Santiago
e-mail: javier.alonso@inaf.it

* Based on observations made with the Italian Telescopio Nazionale Galileo (TNG) operated on the island of La Palma by the Fundación Galileo Galilei of the INAF (Istituto Nazionale di Astrofisica) at the Observatorio del Roque de los Muchachos.

called Radcliffe Wave (RW), is a narrow (aspect ratio 1:20) and 2.7-kpc long band with a wave-like shape that, at its closest part, is 300 pc from the Sun (Alves et al. 2020). Its origin can be due to a disc instability (Fleck 2020) or to a perturbation generated by the passage of a satellite (Li & Chen 2022; Thulasidharan et al. 2022).

Many of the most important star forming regions (SFRs) in the solar vicinity, such as Canis Major, Monoceros R2, Orion, Taurus, Perseus, Cepheus, North America nebula and Cygnus are aligned in the XY Galactic plane along the RW, which could be associated to the Orion spiral arm (Swiggum et al. 2022). It should be noted that four of these complexes (Orion, Taurus, Perseus and Cepheus) have classically been part of the Gould Belt (Gould 1874; Palouš & Ehlerová 2017). It was assumed to be a Sun-centred ring-shaped structure with a size of about 500 pc involving the nearest molecular clouds and OB associations as well as a sparse population of X-ray point-like sources associated with young stellar objects (YSOs) (e.g., Guillout et al. 1998). However, in light of *Gaia*'s very precise astrometry, our view of the Gould Belt has changed, becoming in fact just the apparent projection on the sky of two larger physical structures: the RW and the 'split' (Alves et al. 2020; Swiggum et al. 2022). The latter is also a linear arrangement of cloud complexes 1 kpc long and contains, among others, the Ophiucus SFR, the only one of the five large Gould clouds not associated to the RW.

Since its discovery, the kinematics of the RW has been studied to investigate the possible existence of an oscillation pattern. Different RW tracers such as YSOs, OB stars, young OCs or even masers and radio sources were used, which, however, did not lead to conclusive results (Donada & Figueras 2021; Bobylev et al. 2022; Li & Chen 2022; Thulasidharan et al. 2022; Tu et al. 2022; Alfaro et al. 2022; Bobylev & Bajkova 2024). Finally, Konietzka et al. (2024), by making use of line-of-sight velocity measurements of ^{12}CO and 3D velocities of young OCs, demonstrated that the RW is not only sinusoidal in shape but actually oscillates across the Galactic plane and moves radially outward from the Galactic centre. It implies that all the SFRs composing the RW share a common history. In fact, it is possible that the star cluster whose supernovae originated the Local Bubble was also part of the RW in the past (Zucker et al. 2022).

In this context, the RW and its individual components constitute an unparalleled laboratory for the study of star formation in the solar neighbourhood. Indeed, metal mixing in giant molecular clouds is key to understanding the star formation history and the chemical evolution of the Galaxy. Traditionally, the nearby molecular clouds were assumed to be well mixed. However, De Cia et al. (2021) observed nearby hot, young stars and found differences of a factor of ten in metallicity, which was ascribed to inhomogeneous metal mixing in the natal cloud(s), on a scale of a few parsec to tens of parsec at most. Whether inhomogeneous mixing is a general feature should be ascertained by looking at molecular clouds systems, such as those defining the RW. In this respect, Fu et al. (2022), claimed the possible detection of metallicity variations along the Wave in a work based on low-resolution LAMOST spectra of OCs stars.

To date, the RW has always been studied from a kinematical perspective. This work represents the first attempt to characterise its chemical pattern. The use of high-resolution spectroscopy to derive precise chemical abun-

dances of some young OCs associated to the Wave can shed light on the gas mixing and star formation processes inside the structure. Given the young age of the Wave, we expect that stellar evolution and migration across the Galactic disc have not significantly affected the clusters yet and, thus, their chemical composition should be representative of the composition of the local gas. The analysis of elements belonging to all main nucleosynthesis channels allows us to establish the chemical coherence of OCs belonging to the RW, and to estimate local enrichment effects due, for instance, to recent supernovae explosions. We might expect that star formation had propagated in nearby clusters and that the formation of stars in one subgroup might trigger or affect star formation in the other subgroups (e.g., Armillotta et al. 2018).

The paper is structured as follows. In Sect. 2 we present our observations and the criteria used to select our targets. The spectral analysis that we followed is described in Sect. 3 along with the stellar parameters and chemical abundances we obtained. The chromospheric activity and the lithium content are evaluated in Sect. 4. Then, we compare our results with the literature and place them in the Galactic context in Sect. 5, while the discussion and interpretation of our findings relative to the Radcliffe Wave are presented in Sect. 6. Finally, in Sect. 7 we summarize our results and present our conclusions.

2. Observations and data reduction

To study the RW, instead of relying on field stars (for which the age is always difficult to measure with a sufficient precision) or on molecular gas (due to the uncertainties in determining its chemical and kinematical properties), it is convenient to use young OCs as tracers. For those, one can obtain a robust age determination and precise kinematics and element abundances. Many candidate clusters have been proposed to be associated to the Wave (e.g., Donada & Figueras 2021; Fu et al. 2022). As stars in a cluster share essentially the same age, initial metallicity and chemical composition, observations of a few members is sufficient to characterise the cluster, as already shown in some papers based on data of the Stellar Populations Astrophysics (SPA) large program conducted at the TNG. In those papers, we have chemically characterised a sample of dwarfs and giants in nearby OCs using high-resolution spectra (e.g., Frasca et al. 2019; Casali et al. 2020; D'Orazi et al. 2020; Alonso-Santiago et al. 2021; Zhang et al. 2021, 2022).

2.1. Sample selection

We have initially selected five nearby and low-extinction OCs associated with the RW, namely Melotte 20 (α Per), Pleiades (Melotte 22), ASCC 16, NGC 2232, and Roslund 6. To measure the metallicity and abundance ratios with a precision sufficient to resolve cluster-to-cluster variations, we need to use high-resolution spectra of slow rotators ($v \sin i \leq 10\text{--}15 \text{ km s}^{-1}$; higher rotation would blur and blend lines). In these young OCs, this means observing main-sequence (MS) stars of mid-G spectral type. To this aim, we have selected four to six members of the above clusters from the lists of Cantat-Gaudin et al. (2020) with a color index ($G_{\text{BP}} - G_{\text{RP}}$) in the range 0.75–0.95 mag, corresponding approximately to G1–G9 spectral types, which

have no visual companion with a comparable magnitude within $10''$. To reject fast-rotating stars, which are frequent in young ($age < 300$ Myr) clusters (e.g., Barnes 2003; Fritzewski et al. 2020), we have initially relied on the spectral line broadening parameter V_{broad} , which is reported in the *Gaia* DR3 catalogue (Gaia Collaboration et al. 2023) and is based on the medium-resolution *Gaia* RVS spectra (Frémat et al. 2023). This parameter is not available for all the pre-selected targets. Moreover, it provides only a rough indication of line broadening, due to the moderate resolution ($R=11,500$) of RVS and the presence of broad Ca II IRT lines in its spectral domain. Therefore, we have used an inclusive threshold of $V_{\text{broad}} \leq 40 \text{ km s}^{-1}$ and resorted to additional criteria to select the slowly-rotating stars. For the pre-selected sources, we have retrieved from the MAST¹ archive the light curves produced by the NASA’s Transiting Exoplanet Survey Satellite (*TESS*; Ricker et al. 2015) and searched for the rotation period, P_{rot} by means of the periodogram analysis (Scargle 1982) and the CLEAN deconvolution algorithm (Roberts et al. 1987), similar to what we did in Frasca et al. (2023a). We have then chosen the targets with the longest period ($P_{\text{rot}} \geq 3$ d) for which an equatorial velocity $v_{\text{eq}} \leq 16 \text{ km s}^{-1}$ is expected. For the Pleiades we used the rotational periods derived by Rebull et al. (2016) for a sample of members observed with *Kepler*-K2. These selection criteria do not prevent some binary system from being included. Indeed, four double-lined spectroscopic binaries (SB2s) were observed and their spectra were also used, as discussed in Sect. 3.

In addition to the solar-type stars, a few brighter and faster rotating F5–G0 type stars have been observed as well. For them, a value of $v \sin i \leq 60 \text{ km s}^{-1}$ is a safe threshold for determining the atmospheric parameters, $v \sin i$, and RV with a sufficient precision with ROTFIT, as we did in Frasca et al. (2019) and Alonso-Santiago et al. (2021), where we were also able to derive parameters for binary systems.

We have increased our target sample with archive spectra of two members of NGC 2232 and three members of Melotte 20, as well as several stars in three additional OCs associated with the RW, namely ASCC 19, NGC 7058, and ASCC 123. Spectra of these sources were taken in the framework of the SPA large program before this structure was discovered by Alves et al. (2020). However, the selection criteria for the candidate members of these three clusters are different, with the result of including more hotter and faster rotating stars. The analysis of ASCC 123 was previously published in a dedicated paper and will not be further discussed throughout the present work. The reader can find all the information in Frasca et al. (2019, 2023a).

The main properties of the clusters targeted in this work, according to Cantat-Gaudin et al. (2020), are reported in Table 1. Additionally, Fig. 1 shows the position on the color-magnitude diagram (CMD) of the likely members observed in each cluster. Note that five of these clusters (ASCC 16, ASCC 19, NGC 2232, NGC 7058, and Roslund 6) have not been studied with high signal-to-noise ratio (S/N), high resolution before, while Melotte 20 and Pleiades have been included in this study to compare with literature and keep systematics under control. ASCC 123 is also a very little-studied cluster whose only chemical study to date was carried out, as we have already mentioned, by our group.

Table 1. Main properties of the clusters investigated in this work according to Cantat-Gaudin et al. (2020): radius containing half of the members ($r50$), number of high-probability members (N), age ($\log \tau$), extinction (A_V) and average distance (d).

Cluster	$r50$ (°)	N	$\log \tau$	A_V	d (pc)
Melotte 20 / α Per	2.027	747	7.71	0.30	171
Pleiades / Melotte 22	1.274	952	7.89	0.18	128
ASCC 16*	0.376	175	7.13	0.20	344
ASCC 19	0.605	149	7.02	0.13	346
NGC 2232	0.516	188	7.25	0.01	315
Roslund 6	1.004	247	7.95	0.00	375
NGC 7058	0.109	26	7.61	0.18	350
ASCC 123	1.294	49	7.65	0.00	229

Note. * Identified as Briceno 1 in Hunt & Reffert (2023) and Cavallo et al. (2024).

In total, we observed 59 stars that are listed in Table 2. We followed an internal numbering that consists of adding a sequential number to the (short)name of the cluster to which they belong. For Melotte 20 and NGC 2232, we distinguished between the stars observed during the main run (letter S) and those taken from the SPA archive (A). Not all the targets in our preliminary list were observed and that is why some numbers are missing. In any case, to facilitate their identification we also provide the *Gaia* source name in Table 2 and the equatorial coordinates (J2000.0) in Table A.1.

2.2. Spectroscopic observations

The observations were conducted from 26 to 28 October 2022 and in the fall of 2019 and 2020 for those collected in the framework of the SPA large program (see Table 2 for a logbook of the observations). We used the GIARPS (GIANO-B & HARPS-N; Claudi et al. 2017) facility at the 3.6m TNG telescope located at El Roque de los Muchachos Observatory, in La Palma (Spain). With GIARPS we are able to simultaneously collect both optical (HARPS-N, $R \simeq 115\,000$, range = $0.39\text{--}0.68 \mu\text{m}$, Cosentino et al. 2014) and near-infrared (NIR) high-resolution spectra (GIANO-B, $R \simeq 50\,000$, range = $0.97\text{--}2.45 \mu\text{m}$; Oliva et al. 2012; Origlia et al. 2014). The HARPS-N spectra were acquired with the second fiber on-sky. The total exposure times ranged from 300 to 7200 sec, depending on the star brightness and sky conditions, and were chosen so as to reach a signal-to-noise ratio per pixel $S/N \geq 30$ at red wavelengths. Exposures longer than 1800 sec were usually split in two or three to reduce the contamination of cosmic rays. The coordinates, TIC identifier, as well as the main kinematical properties of the stars observed at the TNG are listed in Table A.1. In the present paper we only make use of HARPS-N spectra, which are best suited for the determination of stellar parameters and abundances of solar-like stars.

The HARPS-N spectra were reduced by dedicated personnel using the instrument Data Reduction Software pipeline. Radial velocities (RVs) were derived by this pipeline using the weighted cross-correlation function (CCF) method (Baranne et al. 1996; Pepe et al. 2002). However, we preferred to perform an ad-hoc CCF analysis using

¹ <https://mast.stsci.edu/portal/Mashup/Clients/Mast/Portal.html>

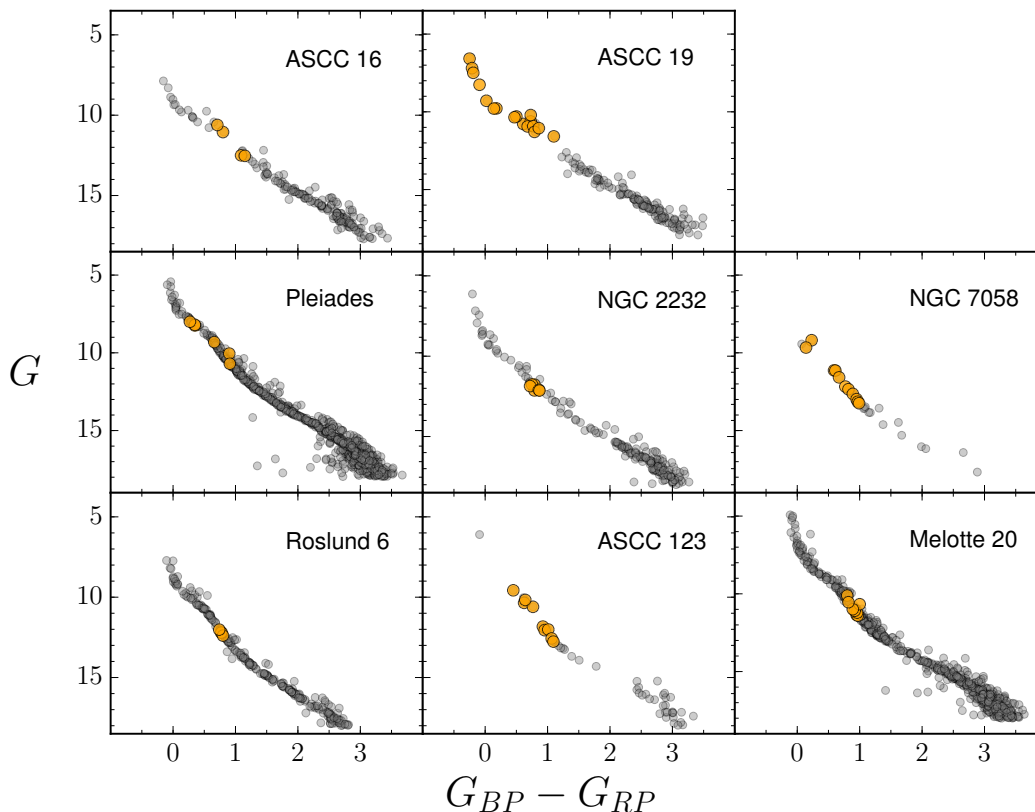


Fig. 1. CMDs of the clusters studied in this work. Small grey circles represent the likely members identified in Cantat-Gaudin et al. (2020) while the big orange ones mark the stars composing our sample for which we have GIARPS spectra.

synthetic template spectra and a broader RV window because some of our targets turned out to be spectroscopic binaries or rapidly rotating stars whose CCF peaks were not entirely covered by the RV range of the online CCF procedure. The telluric H_2O lines at the $\text{H}\alpha$ and NaID_2 wavelengths, as well as those of O_2 at 6300 \AA , were removed from the extracted HARPS-N spectra using an interactive procedure described in Frasca et al. (2000) and adopting telluric templates (spectra of hot, fast-rotating stars) acquired during the observing run. For the following analysis we have normalized the spectra to the local continuum by fitting a low-order polynomial.

3. Stellar parameters and abundances

3.1. Radial velocity

We begin our spectroscopic analysis by measuring the RV, which is obtained by cross-correlating the HARPS-N spectra of our targets with synthetic BTSettl templates (Allard et al. 2012). The cross-correlation is carried out separately for 14 spectral segments of 200 \AA each, from 4000 \AA to 6800 \AA , after masking emission lines and regions strongly affected by telluric absorption lines. The model spectrum producing the highest correlation peak is degraded to the spectral resolution of HARPS-N and resampled to the spectral points of the target spectrum. To measure the centroid of the cross-correlation peak, we fitted it with a Gaussian by the procedure CURVEFIT (Bevington & Robinson 2003), taking the CCF noise, σ_{CCF} , into account. The latter was

evaluated as the standard deviation of the CCF values in two windows at the two sides of the peak. The RV error per each segment, σ_{RV} , was estimated as the error of the centre of the Gaussian fitted to the CCF (see also Frasca et al. 2017). The RV and associated uncertainty were computed as the weighted mean and weighted standard deviation of the RVs obtained from individual segments, adopting $w = 1/\sigma_{\text{RV}}^2$ as the weight. For the components of a SB2 we evaluated the RVs by means of a two-Gaussian fit. As a check, we used also the IRAF² task FXCOR for a few targets, obtaining values and errors in close agreement with those determined with our procedure. The RV values are listed in Table 3 for the single (or single-lined) stars and in Table 4 for the components of SB2 systems. For the latter we also estimated the systemic velocity, γ , following the guidelines of Frasca et al. (2019, Eq. 1).

Stars belonging to the same cluster share a similar RV and this is what we see for most of the stars in Table 3. However, stars A1 and S3 in Melotte 20 and S1, S2, and S9 in NGC 7058 show somewhat different RVs with respect to the other cluster members. We note that Mel20-A1 was not selected on the basis of *Gaia* data and came out as a non-member on the basis of our chemical analysis. The remaining four stars are bona fide members according to both Cantat-Gaudin et al. (2020) and Hunt & Reffert (2023). Ad-

² IRAF is distributed by the National Optical Astronomy Observatory, which is operated by the Association of the Universities for Research in Astronomy, Inc. (AURA), under cooperative agreement with the National Science Foundation.

Table 2. Observation log.

Star ^a	<i>Gaia</i> DR3 source	Date_obs yyyy-mm-dd	UT_mid hh:mm	t_{exp} (s)	S/N ^b
Mel20-A1	435977186717605504	2019-08-11	05:34	1380	54
" "	435977186717605504	2019-08-14	05:51	1380	69
Mel20-A2	436477017829810944	2019-08-12	05:28	3000	47
Mel20-A3	441585726810505472	2019-08-15	04:54	3000	106
Mel20-S1	247787692782638976	2022-10-27	00:27	3600	74
Mel20-S2	441466189279599104	2022-10-27	01:21	2400	67
Mel20-S3	461768327888957440	2022-10-28	00:20	1800	66
Mel20-S8	442036938892925824	2022-10-28	00:53	1500	63
Mel20-S11	244833446777247488	2022-10-28	01:16	900	76
Plei-S2	65199978672758272	2022-10-26	23:42	1200	80
Plei-S3	64808204638390912	2022-10-27	23:20	700	84
Plei-S5	68129764842889600	2022-10-27	23:45	1500	75
Plei-S7	66715273197982848	2022-10-26	23:13	300	78
Plei-S8	68293729514855040	2022-10-26	23:27	300	86
Plei-S9	68306099020642432	2022-10-29	03:23	900	153
ASCC16-S1	3222084843416897664	2022-10-28	02:16	5400	57
ASCC16-S2	3222099274507005056	2022-10-27	02:55	3600	37
ASCC16-S6	3222160885813451776	2022-10-27	02:07	1800	53
ASCC16-S12	3221874669193382016	2022-10-28	05:17	1200	64
ASCC19-S1	3217109248360315904	2019-11-09	06:11	2800	66
ASCC19-S2	3220091879809599616	2019-11-11	05:11	2800	60
ASCC19-S3	3214057416398183296	2019-11-11	06:04	2800	52
ASCC19-S4	3220302676802812928	2019-11-12	06:09	2800	12
ASCC19-S5	3220244986802246400	2020-09-29	04:58	4260	96
ASCC19-S6	3220215162549378176	2020-10-01	05:28	2840	82
ASCC19-S7	3220189976861927808	2020-10-01	06:10	4260	65
ASCC19-S14	3220092532644062720	2019-12-08	01:55	4500	70
ASCC19-S15	3217211812178947072	2019-12-08	04:00	4500	71
ASCC19-S16	3217189753227270144	2020-09-29	06:06	4420	126
ASCC19-S17	3217072174202699264	2019-12-08	22:23	690	81
ASCC19-S18	3220290376016482304	2019-12-08	22:38	690	77
ASCC19-S19	3217081898008606464	2019-12-08	23:22	690	56
ASCC19-S20	3214070301300036992	2020-10-01	04:48	1400	166
ASCC19-S21	3220707468880621568	2020-10-02	03:27	1400	74
ASCC19-S22	3220110983823622400	2019-12-09	00:22	4200	23
ASCC19-S23	3210985999385616000	2020-10-02	04:19	2800	91
NGC2232-A2	3104532761057366016	2020-11-25	02:11	6300	68
NGC2232-A3	3104339964265249536	2020-11-25	04:29	6300	83
NGC2232-S3	3104457096612037504	2022-10-27	04:17	5400	47
NGC2232-S4	3104591653648488192	2022-10-27	05:20	1800	41
" "	" "	2022-10-28	04:47	1800	43
" "	" "	2022-10-29	04:53	1800	33
NGC2232-S9	3104453905456953216	2022-10-28	03:27	3600	54
NGC2232-S11	3104153120306292096	2022-10-29	04:53	2100	46
Ros6-S1	2058141112700761472	2022-10-26	20:33	7200	62
Ros6-S2	2061151889077202688	2022-10-26	22:14	3600	46
Ros6-S5	2064092361123030912	2022-10-27	20:52	7200	49
Ros6-S9	2067418413856205056	2022-10-27	22:33	3600	58
NGC7058-S1	2171977885162801920	2019-08-11	03:25	1380	75
NGC7058-S2	217197782083589888	2019-08-11	03:58	2070	78
NGC7058-S3	2172020903547164416	2019-08-11	21:46	2760	48
NGC7058-S4	2171979843667676416	2019-08-11	22:38	2760	47
NGC7058-S5	2171976510773081728	2019-08-12	02:11	2760	32
NGC7058-S6	2172072370130551936	2019-08-12	03:07	3000	25
NGC7058-S7	2171979427039771648	2019-08-15	00:42	3600	29
NGC7058-S9	2171974827145934464	2019-08-16	01:19	3600	16
NGC7058-S10	2171977782083591680	2019-08-14	01:52	5550	29
NGC7058-S11	2171929747167359488	2019-08-14	00:13	5550	38
NGC7058-S12	2171982145770310528	2019-08-12	00:50	5520	19
" "	" "	2019-08-14	05:15	1980	20
NGC7058-S13	2171970497818874368	2019-08-15	23:45	6300	22

Notes. ^a "Internal" identifier. ^b Signal-to-noise ratio per pixel at 6500 Å.

ditionally, Mel20-S3 and NGC7058-S9, cool stars for which we derived the abundances (Sect. 3.3), show a chemical composition fully compatible with that of their respective clusters. On the other hand, the warm star Plei-S8, despite

having an RV compatible with that of the cluster, is not included in the list of Cantat-Gaudin et al. (2020) and has a low membership probability, Prob=0.2, according to Hunt & Reffert (2023).

3.2. Atmospheric parameters

The second step of our analysis is the determination of the stellar atmospheric parameters (APs) namely, effective temperature (T_{eff}), surface gravity ($\log g$) and metallicity (using $[\text{Fe}/\text{H}]$ as a proxy). For the stars with single-lined HARPS-N spectra, APs were derived with the code ROTFIT (Frasca et al. 2006), which also allows us to measure the projected rotational velocity ($v \sin i$) and to perform an MK spectral classification (SpT). ROTFIT uses a grid of template spectra and is based on a χ^2 minimization of the difference *observed–template* in 28 selected spectral regions of 100 Å each in which we split our HARPS-N spectra. As templates, we adopted high-resolution ELODIE spectra of real stars, whose APs are well-known. This grid is the same used by the Catania (OACT) node for the analysis of FGK-type spectra in the *Gaia*-ESO Survey (GES; see, e.g., Smiljanic et al. 2014; Frasca et al. 2015). The spectra of our targets are degraded to the resolution of ELODIE ($R = 42\,000$) and resampled on the ELODIE spectral points ($\Delta\lambda = 0.05$ Å). This also has the advantage of improving the S/N of the spectra to be analyzed. For a detailed description of the application of ROTFIT to the HARPS-N spectra the reader is referred to Frasca et al. (2019). An example of the application of the code ROTFIT to two spectral segments of ASCC16-S2 is shown in Fig. 2.

For the hottest stars, those near or beyond the early-type edge of the ELODIE template grid ($\approx F0$), we used a different approach, as done in previous works (see for example Alonso-Santiago et al. 2024). For these objects, we made use of synthetic templates (see Sect. 3.3) and focused on the wings and cores of the Balmer lines, which are efficient diagnostics of $\log g$ and T_{eff} respectively, as well as additional spectral regions with weaker lines to constrain the $v \sin i$, mainly the Mg I $\lambda 4481$ Å, clearly visible at these effective temperatures.

As mentioned above, the observed targets include four SB2 systems. One of these, Plei-S2 (= HII 1117 = HD 282975), was already discovered as a double-lined spectroscopic binary by Mermilliod et al. (1992), but we decided to keep it in our list and observe it anyway for comparison purposes. Another SB2, NGC2232-S4, was discovered by us as an eclipsing binary by examination of *TESS* light curves and was observed purposely to obtain high-precision stellar parameters which were the subject of a recent work (Frasca et al. 2023b).

The spectral lines of the components of these SB2s are sufficiently separated in wavelength to allow us to infer their stellar parameters from a proper analysis of their spectra. For the SB2 in NGC2232 (TIC 43152097), which is also a totally eclipsing binary, we have already provided the parameters of the two components in Frasca et al. (2023b) by simultaneously solving the RV and light curves. To get the stellar parameters for SB2 systems, we used COMPO2, a code developed in IDL³ environment by Frasca et al. (2006), which, like ROTFIT, was adapted to the HARPS-N spectra. A description of this version of COMPO2 can also be found in Frasca et al. (2019) to which paper the reader is referred to for further details. The continuum flux ratio (i.e., the flux contribution of the primary component in units of the continuum, w^{P}) is an adjustable parameter, which is also

³ IDL (Interactive Data Language) is a registered trademark of Harris Corporation.

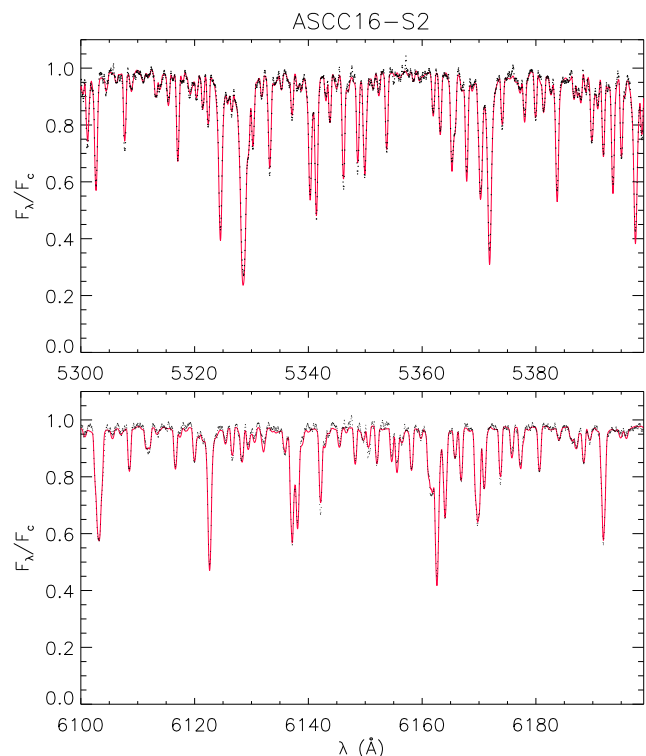


Fig. 2. Observed HARPS-N spectrum of ASCC16-S2 (black dots) in the $\lambda 5300$ Å (*upper panel*) and $\lambda 6100$ Å (*lower panel*) spectral regions. In each panel the template spectrum broadened at the $v \sin i$ of the target is overlaid with a full red line.

an output of the code. An example of the application of COMPO2 to the binary Mel20-S11 is shown in Fig. 3 for two spectral segments, one around the Mg I b triplet and the other centred at 6440 Å, in which the lines of the two components are clearly distinguishable. The flux contribution was evaluated at three wavelengths (4400 Å, 5500 Å, and 6400 Å) using only the spectral segments around these wavelengths. In this case, the SpTs of the components are taken as the mode of the spectral-type distributions, while the APs are estimated as the weighted averages of the best 100 combinations per each analyzed spectral segment, considering the χ^2 and the line intensity in the weight. The APs obtained for the single stars are reported in Table 3, in which we also list the rotational periods measured by analyzing the *TESS* light curves, while those for SB2s systems are listed in Table 4.

3.3. Elemental abundances

Once the APs are known, we can determine the chemical abundances. We followed the same strategy implemented in our previous works (Alonso-Santiago et al. 2021, 2024; Catanzaro et al. 2024), which is based on the spectral synthesis technique (Catanzaro et al. 2011, 2013). We focused only on cool stars, those with $T_{\text{eff}} < 7500$ K, since the fast rotation in hotter stars with earlier B–A types blurs the spectral lines, preventing a reliable estimate of abundances. Additionally, in these stars, compared to cool ones, the number of spectral features is also smaller.

Table 3. Stellar parameters of the single-lined members of Radcliffe Wave clusters derived in the present work with the code ROTFIT.

Star	T_{eff} (K)	$\log g$ (dex)	[Fe/H] (dex)	SpT	$v \sin i$ (km s ⁻¹)	RV (km s ⁻¹)	P_{rot}^a (d)	Memb?
Mel20-A1	5752 ± 69	4.35 ± 0.12	0.19 ± 0.07	G2.5V	1.9 ± 1.4	-5.98 ± 0.07	...	N
Mel20-A2	5843 ± 71	4.44 ± 0.11	-0.03 ± 0.10	G1V	11.6 ± 0.4	-1.62 ± 0.12	4.08	Y
Mel20-A3	6101 ± 70	4.20 ± 0.10	0.09 ± 0.08	F8V	4.4 ± 0.8	-0.68 ± 0.06	2.64	Y
Mel20-S1	5774 ± 71	4.37 ± 0.12	0.06 ± 0.08	G2V	8.2 ± 0.5	1.71 ± 0.08	3.98	Y
Mel20-S2	5781 ± 74	4.41 ± 0.12	0.10 ± 0.09	G2V	11.9 ± 0.3	0.41 ± 0.18	3.26	Y
Mel20-S3	5888 ± 110	4.44 ± 0.11	-0.03 ± 0.10	G1V	14.2 ± 0.3	-4.34 ± 0.16	3.90	Y?
Mel20-S8	5828 ± 72	4.44 ± 0.11	-0.02 ± 0.10	G2V	13.5 ± 0.5	-0.88 ± 0.15	3.05	Y
Plei-S3	6601 ± 119	4.14 ± 0.15	-0.00 ± 0.07	F6V	34.4 ± 1.2	5.96 ± 0.59	6.16 ^b	Y
Plei-S5	5752 ± 67	4.39 ± 0.12	0.18 ± 0.08	G2V	9.3 ± 0.3	5.54 ± 0.12	6.84 ^b	Y
Plei-S7*	7800 ± 170	3.90 ± 0.20	-0.20 ± 0.11	A7III	18.4 ± 6.8	4.99 ± 0.23	...	Y
Plei-S8*	7900 ± 160	3.90 ± 0.20	-0.16 ± 0.11	A7III	31.8 ± 6.2	4.31 ± 0.43	...	N
Plei-S9*	8200 ± 100	4.10 ± 0.20	-0.20 ± 0.15	A4IV	40.7 ± 6.2	4.35 ± 1.02	...	Y
ASCC16-S1	5271 ± 89	4.53 ± 0.13	-0.00 ± 0.08	K0V	17.9 ± 0.4	21.27 ± 0.37	4.15	Y
ASCC16-S2	5184 ± 84	4.54 ± 0.10	-0.03 ± 0.08	K0V	18.3 ± 0.4	20.57 ± 0.34	4.06	Y
ASCC16-S6	5947 ± 114	4.34 ± 0.13	0.07 ± 0.08	G2V	32.5 ± 0.4	21.37 ± 0.43	2.34	Y
ASCC16-S12	6233 ± 107	3.87 ± 0.14	-0.02 ± 0.09	F8IV	32.8 ± 0.6	20.58 ± 0.48	2.82	Y
ASCC19-S1	6724 ± 135	4.14 ± 0.14	-0.02 ± 0.08	F4V	53.5 ± 1.4	22.53 ± 0.52	3.77	Y
ASCC19-S2	6549 ± 170	4.09 ± 0.16	-0.06 ± 0.12	F5V	171.3 ± 7.2	25.16 ± 3.62	0.642	Y
ASCC19-S3	6657 ± 119	4.14 ± 0.15	-0.01 ± 0.08	F4V	110.8 ± 4.4	21.16 ± 1.62	...	Y
ASCC19-S4	6062 ± 119	4.15 ± 0.14	-0.03 ± 0.12	F9IV-V	13.8 ± 0.6	21.76 ± 0.28	4.26	Y
ASCC19-S5	6084 ± 73	4.20 ± 0.10	0.07 ± 0.10	F9IV-V	18.2 ± 1.0	23.89 ± 0.32	3.42	Y
ASCC19-S6	5895 ± 96	4.35 ± 0.14	0.11 ± 0.09	G0V	45.5 ± 1.1	22.71 ± 1.20	2.09	Y
ASCC19-S14	6513 ± 96	3.96 ± 0.12	-0.03 ± 0.09	F4V	17.0 ± 0.7	23.28 ± 0.18	0.665	Y
ASCC19-S15	6988 ± 121	4.13 ± 0.12	-0.04 ± 0.08	F1V	62.6 ± 1.9	22.70 ± 1.01	0.622	Y
ASCC19-S16	6750 ± 220	4.21 ± 0.13	-0.35 ± 0.15	F2V	64.8 ± 4.4	21.29 ± 0.84	...	Y
ASCC19-S17*	16 800 ± 900	4.00 ± 0.15	0.00	B4V	250.0 ± 10.0	22.06 ± 2.10	...	Y
ASCC19-S18*	14 700 ± 600	4.10 ± 0.10	0.00	B6V	38.0 ± 5.0	21.48 ± 0.70	...	Y
ASCC19-S19*	14 600 ± 800	4.00 ± 0.20	0.00	B6V	190.0 ± 10.0	18.85 ± 1.85	...	Y
ASCC19-S20*	12 800 ± 300	4.00 ± 0.15	0.00	B8V	120.0 ± 13.2	23.60 ± 0.75	...	Y
ASCC19-S21*	9300 ± 110	4.10 ± 0.15	0.00	A1V	36.9 ± 2.9	20.81 ± 0.27	...	Y
ASCC19-S22*	9400 ± 190	4.10 ± 0.20	0.00	A1V	49.5 ± 2.9	22.35 ± 0.46	...	Y
ASCC19-S23*	9200 ± 360	4.20 ± 0.25	0.00	A1V	137.4 ± 15.7	23.08 ± 1.34	...	Y
NGC2232-A2	5778 ± 73	4.39 ± 0.12	0.10 ± 0.09	G2V	17.9 ± 0.7	26.12 ± 0.26	2.79	Y
NGC2232-A3	5803 ± 69	4.40 ± 0.12	0.05 ± 0.07	G2V	13.1 ± 0.8	26.73 ± 0.24	3.97	Y
NGC2232-S3	5895 ± 111	4.45 ± 0.10	-0.04 ± 0.10	G1V	17.5 ± 0.4	26.05 ± 0.35	3.11	Y
NGC2232-S9	5849 ± 70	4.44 ± 0.11	-0.04 ± 0.10	G1V	17.6 ± 0.4	25.96 ± 0.32	2.61	Y
NGC2232-S11	6099 ± 75	4.17 ± 0.12	0.06 ± 0.09	F8V	12.1 ± 0.7	26.94 ± 0.14	3.06	Y
Ros6-S1	5942 ± 133	4.45 ± 0.10	-0.03 ± 0.10	G1V	13.7 ± 0.4	-8.13 ± 0.21	3.13	Y
Ros6-S2	6082 ± 71	4.30 ± 0.14	0.05 ± 0.09	G1V	17.3 ± 0.5	-8.20 ± 0.28	2.78	Y
Ros6-S5	5844 ± 68	4.43 ± 0.11	-0.03 ± 0.10	G1V	14.1 ± 0.3	-7.47 ± 0.22	3.24	Y
Ros6-S9	6088 ± 72	4.20 ± 0.10	0.07 ± 0.09	F8V	13.6 ± 0.4	-8.24 ± 0.12	3.27	Y
NGC7058-S1*	9200 ± 200	4.10 ± 0.10	0.00	A1	95.7 ± 2.6	-5.51 ± 2.02	...	Y?
NGC7058-S2*	9500 ± 200	4.30 ± 0.10	0.00	A0	42.3 ± 1.2	-8.05 ± 0.47	...	Y?
NGC7058-S3	6700 ± 148	4.15 ± 0.16	-0.02 ± 0.09	F5V	116.4 ± 5.4	-17.25 ± 3.18	...	Y
NGC7058-S4	6654 ± 122	4.14 ± 0.15	-0.01 ± 0.09	F3V	119.3 ± 4.3	-18.21 ± 2.85	...	Y
NGC7058-S5	6324 ± 147	4.10 ± 0.17	0.00 ± 0.08	F6IV	41.7 ± 2.2	-19.25 ± 1.01	1.48	Y
NGC7058-S6	6087 ± 72	4.21 ± 0.10	0.07 ± 0.10	F8V	24.7 ± 0.8	-19.13 ± 0.40	13.65	Y
NGC7058-S7	5901 ± 120	4.44 ± 0.11	0.05 ± 0.07	G1V	14.8 ± 0.9	-19.03 ± 0.22	2.87	Y
NGC7058-S9	5785 ± 88	4.42 ± 0.12	-0.00 ± 0.10	G2V	6.6 ± 0.5	-33.25 ± 0.08	7.30	Y?
NGC7058-S10	5744 ± 83	4.38 ± 0.12	0.18 ± 0.08	G2V	4.0 ± 0.7	-19.41 ± 0.07	6.77	Y
NGC7058-S11	5682 ± 114	4.45 ± 0.15	0.19 ± 0.10	G2.5V	5.8 ± 0.4	-19.43 ± 0.07	4.63	Y
NGC7058-S12	5491 ± 157	4.53 ± 0.11	0.11 ± 0.11	K0V	7.5 ± 0.5	-19.08 ± 0.09	4.82	Y
NGC7058-S13	5285 ± 90	4.55 ± 0.11	-0.00 ± 0.09	K0V	3.3 ± 0.8	-18.96 ± 0.06	5.69	Y

^a Rotation periods derived in the present paper analyzing the *TESS* light curves.

^b Rotation periods derived by Rebull et al. (2016) with *Kepler-K2*.

* Warm stars. Atmospheric parameters derived with synthetic templates with solar metallicity as described in the text.

As a first step we computed the atmospheric model for each star from their APs, previously obtained with ROTFIT (Sect. 3.2). We produced 1D local thermodynamic equilibrium (LTE) models by means of the ATLAS9 code (Kurucz 1993a,b) and then the corresponding synthetic spectra

were generated using the radiative transfer code SYNTHE (Kurucz & Avrett 1981). The next stage of our analysis consisted of comparing the target spectra (at their original resolution) with the synthetic ones (adequately broadened according to the instrumental and rotational profiles).

Table 4. Stellar parameters of the components of SB2 systems derived with the code COMPO2.

Star	T_{eff} (K)	err (K)	$\log g$ (dex)	err (dex)	RV (km s ⁻¹)	err (P/S)	γ (km s ⁻¹)	w_{4400}^P	w_{5500}^P	w_{6400}^P	SpT (P/S)	$v \sin i$ (km s ⁻¹) (P/S)
Mel20-S11	6119/5172	75/240	4.02/3.92	0.14/0.62	31.74/-41.46	0.15/2.39	4.2±1.2	0.91±0.02	0.89±0.02	0.90±0.03	F7IV/K1IV	8/8
Plei-S2	5674/5371	139/172	4.36/4.39	0.13/0.14	14.32/0.20	0.22/0.30	7.4±0.2 ^a	0.56±0.03	0.55±0.03	0.53±0.03	G2V/G2V	4/3
ASCC19-S7	5376/4894	139/226	4.41/4.36	0.11/0.40	35.49/9.11	0.25/1.16	24.6±0.5	0.87±0.02	0.83±0.02	0.79±0.04	G8V/K4V	7/7

^a In very good agreement with the value of 7.434 km s⁻¹ reported by Torres et al. (2021).

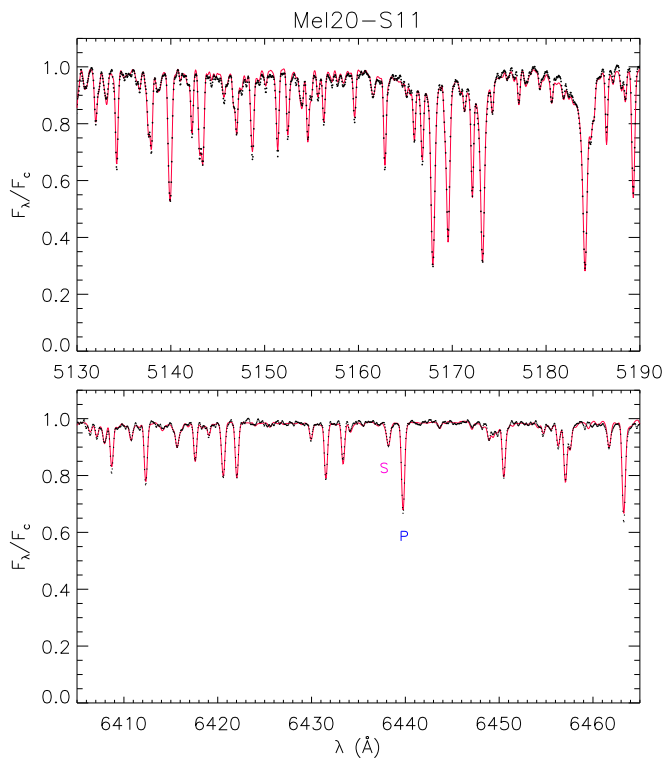


Fig. 3. Observed HARPS-N spectrum of the SB2 system Mel20-S11 (black dots) around the Mg I b lines (λ 5160 Å, *upper panel*) and around λ 6440 Å (*lower panel*). In each panel the synthetic spectrum, which is the weighted sum of two standard star spectra mimicking the primary and secondary component of Mel20-S115, is overplotted with a full red line.

This was carried out in 39 spectral segments of 50 Å each between 4400 and 6800 Å. The chemical abundances were then found by minimizing the χ^2 of their differences. The final abundance of each element was estimated as the mean of the individual values from all the observed spectral lines, after applying a 2σ -clipping to remove outliers. The median absolute deviation of the individual abundances was considered a robust indicator of the uncertainty of the average value.

In this way we calculated the chemical abundances of 41 FGK-type stars belonging to the seven clusters under study. We explored 25 elements with atomic numbers up to 60, namely, C, Na, Mg, Al, Si, S, Ca, Sc, Ti, V, Cr, Mn, Fe, Co, Ni, Cu, Zn, Sr, Y, Zr, Ba, La, Ce, Pr, and Nd. We adopted the lines list from Romaniello et al. (2008)

for Fe I and Fe II while for the rest of the elements we used those of Castelli & Hubrig (2004), who updated the original parameters of Kurucz & Bell (1995). Our abundances are always expressed taking as reference the solar composition reported by Grevesse et al. (2007). The individual stellar abundances, in terms of $[X/H]$, are listed in Tables from A.2 to A.6. The chemical composition of the clusters, instead, is reported in Table 5. The final value for each element has been calculated as the weighted average of the abundances of the cluster members (i. e., ‘Y’ and ‘Y?’ stars in Table 3), using the individual errors as weights. Its uncertainty has been estimated as the standard deviation observed among the members. In general, this number is close or below 0.1 dex. Only in a few occurrences we found some scatter in the abundance of some elements among the members of the cluster. This is the case of the Pleiades, where we have only analyzed two stars that exhibit some chemical differences for Fe, Cu and Zn. It is worth clarifying that, for the sake of homogeneity, the $[Fe/H]$ obtained with SYNTHE is used throughout the discussion and chemical analysis, while that of ROTFIT (slightly higher than the former) is displayed in Table 5 only for comparison. In any case, both sets of metallicities are compatible within the errors.

We find that Pleiades, ASCC 16 and NGC 7058 show solar metallicity while Melotte 20, ASCC 19, Roslund 6 and NGC 2232 display values about 0.1 dex lower. A spread in metallicity of almost 0.2 dex can be seen among our targets, which is more than one can expect for these clusters with such similar ages and distances. Regarding the chemical abundances we find, on average, solar composition for α - and Fe-peak elements and a mild overabundance of about 0.2 dex for neutron-capture elements. Sulfur and zinc present some differences with respect the general trend. The former exhibits overabundant values (0.2–0.3 dex above the Sun) while the latter is slightly subsolar.

4. Chromospheric emission and lithium abundance

For stars belonging to young clusters both the chromospheric emission (traced by Balmer H α and Ca II H&K lines in the HARPS-N spectra) and lithium absorption can be used to estimate the age (see, e.g., Jeffries 2014; Frasca et al. 2018, and references therein).

To this aim, the photospheric spectra produced by ROTFIT and COMPO2 with non-active, lithium-poor templates were subtracted from the observed spectra of the targets to measure the excess emission in the core of the H α line ($EW_{H\alpha}$). The result of the subtraction of the photospheric template from the observed spectrum in the H α region is shown in Fig. A.7 for the single-lined objects. The resid-

Table 5. Average chemical composition ($[X/H]$), relative to solar abundances found by Grevesse et al. (2007), of the clusters observed in this work.

X	Melotte 20	Pleiades	ASCC 16	ASCC 19	NGC 2232	Roslund 6	NGC 7058
C	0.23±0.17	0.21±0.12	0.24±0.03	0.18±0.05	0.38±0.06	0.39±0.04	0.15±0.16
Na	0.01±0.09	0.08±0.07	0.05±0.04	0.06±0.17	0.03±0.06	0.05±0.05	0.17±0.04
Mg	-0.04±0.07	0.06±0.06	0.03±0.05	-0.05±0.08	-0.01±0.02	0.00±0.04	0.08±0.07
Al	0.12±0.15	0.16±0.08	0.13±0.08	0.17±0.05	0.08±0.07	0.10±0.09	0.14±0.04
Si	-0.14±0.03	-0.07±0.09	-0.05±0.03	-0.05±0.08	-0.10±0.04	-0.07±0.08	-0.10±0.03
S	0.20±0.20	0.26±0.09	0.29±0.03	0.21±0.04	0.29±0.12	0.20±0.11	0.24±0.06
Ca	0.11±0.12	0.07±0.10	0.14±0.07	0.08±0.05	0.13±0.06	0.13±0.06	0.12±0.12
Sc	-0.08±0.03	0.00±0.11	0.06±0.15	-0.07±0.06	0.03±0.02	-0.01±0.08	-0.04±0.09
Ti	-0.03±0.11	0.06±0.16	0.16±0.10	0.02±0.07	0.01±0.08	-0.01±0.07	0.05±0.09
V	0.11±0.07	0.18±0.01	0.15±0.05	0.17±0.10	0.18±0.05	0.11±0.04	0.14±0.08
Cr	0.06±0.10	0.13±0.13	0.11±0.07	0.03±0.12	0.07±0.05	0.10±0.06	0.07±0.11
Mn	0.09±0.09	0.09±0.16	0.12±0.07	-0.01±0.07	0.11±0.03	0.10±0.05	0.09±0.09
Fe	-0.10±0.13	0.03±0.21	0.01±0.10	-0.14±0.15	-0.10±0.10	-0.11±0.08	-0.02±0.10
Co	0.07±0.06	0.17±0.06	0.14±0.07	0.18±0.06	0.10±0.04	0.14±0.04	0.15±0.07
Ni	-0.08±0.07	0.06±0.08	0.03±0.09	-0.06±0.10	-0.08±0.06	-0.06±0.09	0.03±0.05
Cu	-0.06±0.09	-0.04±0.27	-0.04±0.11	-0.12±0.12	-0.02±0.14	-0.07±0.02	-0.03±0.10
Zn	-0.25±0.11	-0.27±0.20	-0.12±0.16	-0.28±0.10	-0.28±0.07	-0.24±0.05	-0.16±0.09
Sr	0.17±0.08	0.09±0.11	0.15±0.08	0.12±0.13	0.06±0.05	0.10±0.03	0.15±0.13
Y	0.20±0.07	0.19±0.13	0.23±0.11	0.07±0.14	0.22±0.07	0.19±0.02	0.12±0.08
Zr	0.10±0.06	0.22±0.08	0.16±0.10	0.16±0.04	0.15±0.03	0.13±0.03	0.13±0.06
Ba	0.31±0.20	0.27±0.04	0.27±0.15	0.24±0.08	0.47±0.06	0.24±0.05	0.30±0.06
La	0.23±0.05	0.28±0.04	0.28±0.07	0.22±0.04	0.25±0.04	0.26±0.06	0.25±0.11
Ce	0.09±0.04	0.17±0.02	0.15±0.13	0.18±0.05	0.15±0.07	0.12±0.05	0.14±0.10
Pr	0.13±0.05	0.18±0.04	0.15±0.05	0.21±0.01	0.19±0.06	...	0.24±0.14
Nd	0.22±0.07	0.25±0.05	0.21±0.03	0.16±0.03	0.20±0.06	0.23±0.07	0.25±0.06
Fe*	0.01±0.11	0.08±0.13	0.00±0.05	-0.02±0.13	0.03±0.06	0.02±0.05	0.05±0.08

* ROTFIT metallicity, for comparative purpose.

ual emission in the $H\alpha$ core that has been integrated to get $EW_{H\alpha}$ is shown by the hatched green areas in these plots. The equivalent width of the $Li\ I\ \lambda 6708\ \text{\AA}$ absorption line (EW_{Li}) was also measured in the subtracted spectra where the blends with nearby photospheric lines have been removed. The values of $EW_{H\alpha}$ and EW_{Li} are quoted in Tables 6 and 7, respectively.

For SB2 systems, spectral subtraction is strongly advisable to try to isolate chromospheric emission originating from the two components and to remove different lines of the two stars which, due to the Doppler shifts, can overlap the $Li\ I$ line of one or both components. The difference spectrum contains only the $Li\ I$ absorption lines of the two components, whose equivalent widths can be measured individually, eventually by means of a two-Gaussian deblending (see Fig. 4 for an example). We note that the values of EW_{Li} for the components of SB2 systems, which are quoted in Table 7, were corrected by dividing them for the contribution to the continuum of the respective component.

Lithium is a fragile element that is burned in stellar interiors at temperature as low as $2.5 \times 10^6\ \text{K}$. It is progressively depleted from the stellar atmosphere in a way depending on the internal structure (i.e., stellar mass) for stars with convective envelopes deep enough to reach temperatures at which lithium is burned. It can therefore be used as an age proxy for stars cooler than about 6500 K.

We derived the lithium abundance, $A(Li)$, from our values of T_{eff} , $\log g$, and EW_{Li} by interpolating the curves of growth of Lind et al. (2009), which span the T_{eff} range 4000–8000 K and $\log g$ from 1.0 to 5.0 and include non-LTE

corrections. The errors of $A(Li)$ take into account both the T_{eff} and EW_{Li} errors. The values of $A(Li)$ are listed in Table 7.

To estimate or check the ages of the clusters investigated in the present paper from the lithium content in the photospheres of its components, we used the **EAGLES** code (Jeffries et al. 2023). This code fits Li-depletion isochrones to the values of T_{eff} (in the range 3000–6500 K) and W_{Li} of a coeval star group, such as the members of a cluster or a kinematical group or the components of a binary system. We note that **EAGLES** works better for clusters with a wide T_{eff} distribution of members, while in our case most of the stars are solar-like or hotter. The results of the application of this code to our data are shown in Fig. A.8 and summarized in Table 8, along with data from three literature sources, based on *Gaia* data and mass-derivation of ages using automated methods. We also included ASCC 123, whose age was now determined with **EAGLES** for consistency. Its value is younger than the ones previously published in our papers: 100–250 Myr (Frasca et al. 2019, which was derived by isochrone fitting) and a Pleiades-like age (Frasca et al. 2023a, from a gyrochronological perspective). Our results are compatible within the errors with those obtained applying neural networks to photometric data, in a very different approach to ours, in particular with Cantat-Gaudin et al. (2020). ASCC 123 is a peculiar case, as it has been attributed a very large age by Hunt & Reffert (2023) and Cavallo et al. (2024) (more than 1 and 0,6 Gyr, respectively) clearly incompatible with our results, Cantat-Gaudin et al. (2020) and the cluster CMD (see also the age

Table 6. H α and Ca II H&K equivalent widths and fluxes.

Star	$EW_{H\alpha}$ (mÅ)	$F_{H\alpha}$ ($10^5 \text{ erg cm}^{-2} \text{ s}^{-1}$)	$\log(R'_{H\alpha})$	EW_{CaII-K} (mÅ)	EW_{CaII-H} (mÅ)	F_{CaII-K} ($10^5 \text{ erg cm}^{-2} \text{ s}^{-1}$)	F_{CaII-H} ($10^5 \text{ erg cm}^{-2} \text{ s}^{-1}$)	$\log(R'_{HK})$
Mel20-A1	20±36	17±30	1.1±2.0	0.9±1.7	-5.48
Mel20-A2	94±13	7.2±1.0	-4.96	328±73	238±73	20.5±5.2	14.9±4.9	-4.27
Mel20-A3	49±13	4.4±1.2	-5.25	207±39	132±24	19.1±4.0	12.2±2.4	-4.40
Mel20-S1	157±14	11.5±1.1	-4.74	408±58	297±51	23.0±4.0	16.7±3.3	-4.20
Mel20-S2	391±22	28.7±2.1	-4.34	560±60	427±52	31.9±4.8	24.3±3.9	-4.05
Mel20-S3	105±12	8.3±1.1	-4.91	347±78	274±73	23.2±6.5	18.3±5.8	-4.22
Mel20-S8	215±14	16.3±1.3	-4.60	441±62	358±62	26.9±5.0	21.8±4.6	-4.13
Plei-S2 ^a	102±13	7.0±1.1	-4.92	434±80	290±64	23.2±5.3	15.5±4.0	-4.20
Plei-S3	36±6	4.3±0.8	-5.40	149±29	114±28	25.1±5.8	19.1±5.3	-4.39
Plei-S5	73±14	5.3±1.0	-5.07	479±65	330±58	26.2±4.4	18.0±3.6	-4.15
ASCC16-S1	702±24	35.8±2.8	-4.09	1047±137	760±122	26.6±5.5	19.3±4.4	-3.98
ASCC16-S2	661±31	31.3±2.7	-4.12	1262±136	983±152	27.4±5.4	21.3±4.8	-3.92
ASCC16-S6	306±22	25.2±2.6	-4.45	692±78	488±65	49.4±11.0	34.8±8.12	-3.93
ASCC16-S12	55±10	5.3±1.0	-5.20	275±60	201±67	29.3±7.5	21.4±7.7	-4.23
ASCC19-S3	41±15	5.0±1.9	-5.34	235±72	153±64	41.6±13.7	27.0±11.8	-4.21
ASCC19-S4	145±50	12.8±4.5	-4.78	315±343	75±370	27.1±29.9	6-5±31.9	-4.36
ASCC19-S5	72±8	6.4±0.8	-5.08	267±33	189±35	23.6±3.7	16.7±3.5	-4.29
ASCC19-S6	314±13	24.9±2.0	-4.44	655±85	507±73	43.1±8.6	33.3±7.0	-3.95
ASCC19-S7 ^a	3943±190	217±26	-3.34	1774±316	1550±320	68.3±30.8	59.6±27.6	-3.62
ASCC19-S14	29±11	3.3±1.3	-5.49	196±58	175±62	29.4±9.3	26.2±9.8	-4.26
ASCC19-S15	229±63	139±49	56.4±16.2	34.2±12.3	-4.17
ASCC19-S16	1846±39	260±30	-3.70	326±39	270±37	155±34	128±29	-3.67
NGC2232-A2	440±19	32.2±2.0	-4.29	642±56	514±55	35.4±4.9	28.4±4.3	-4.00
NGC2232-A3	173±8	12.9±0.8	-4.70	367±43	298±49	20.9±3.6	17.0±3.5	-4.23
NGC2232-S3	146±20	11.6±1.8	-4.77	410±63	237±52	26.9±6.3	15.5±4.4	-4.21
NGC2232-S4A	109±17 [†]	9.7±1.6	-4.90	268±49	163±48	25.1±5.1	15.2±4.7	-4.28
NGC2232-S4B	1209±247 [†]	16.2±3.6	-4.01	158±42	65±36	14.8±4.12	6.0±3.4	-3.90
NGC2232-S9	138±16	10.6±1.3	-4.80	454±101	280±76	27.8±7.0	17.2±5.1	-4.17
NGC2232-S11	91±10	8.2±1.0	-4.98	318±61	139±41	30.8±6.5	13.4±4.1	-4.25
Ros6-S1	143±17	11.7±1.7	-4.78	326±40	264±46	23.7±6.0	19.2±5.4	-4.22
Ros6-S2	156±21	14.0±2.0	-4.75	296±45	197±38	25.9±4.6	17.2±3.6	-4.25
Ros6-S5	162±16	12.4±1.4	-4.73	399±68	221±66	25.0±5.1	13.9±4.4	-4.23
Ros6-S9	88±11	7.9±1.0	-4.99	437±91	244±56	39.7±9.1	22.1±5.5	-4.10
NGC7058-S5	87±24	8.9±2.6	-5.01	181±77	100±56	22.0±10.1	12.2±7.1	-4.42
NGC7058-S6	115±28	10.3±2.5	-4.88	517±146	200±106	47.2±14.0	18.3±9.9	-4.07
NGC7058-S7	116±27	9.2±2.3	-4.87	197±71	204±78	13.5±5.6	14.1±6.1	-4.40
NGC7058-S9	226±46	16.6±3.5	-4.58	303±209	153±217	17.9±12.6	9.1±12.9	-4.37
NGC7058-S10	65±26	4.7±1.9	-5.12	499±93	262±86	27.6±6.2	14.5±5.1	-4.17
NGC7058-S11	252±31	17.4±2.5	-4.53	475±156	271±120	24.2±9.0	13.8±6.6	-4.19
NGC7058-S12	218±20	13.2±1.9	-4.59	828±74	349±79	36.7±9.3	15.5±5.1	-3.99
NGC7058-S13	146±44	7.5±2.3	-4.77	597±185	253±144	16.3±5.6	6.9±4.1	-4.28

^a Emission from both components has been integrated.

[†] Corrected for the contribution to the continuum flux.

of about 62 Myr derived by Dias et al. 2021). In the *Gaia*-ESO Survey framework, Binks et al. (2021) studied the lithium depletion boundary age for NGC 2232 and found a value of 38 ± 3 Myr, compatible within the errors with ours. They also highlighted the important role played by magnetic activity in young clusters.

As mentioned above, another important diagnostic of chromospheric activity included in the HARPS-N spectra is represented by the emission in the cores of the Ca II H and K lines (see, e.g., Frasca et al. 2010, 2011, and references

therein). The photospheric templates in the Ca II region are made with synthetic BTSettl spectra (Allard et al. 2012), because the ELODIE templates do not contain this wavelength range. Moreover, due to the high sensitivity of these lines to the chromospheric activity, it is very difficult to find spectra of real stars with a pure photospheric profile clean of any chromospheric contribution in the Ca II cores and is preferable to resort to synthetic spectra. These reproduce accurately the Ca II line profiles even in their cores better than they do in the H α cores. The latter are in-

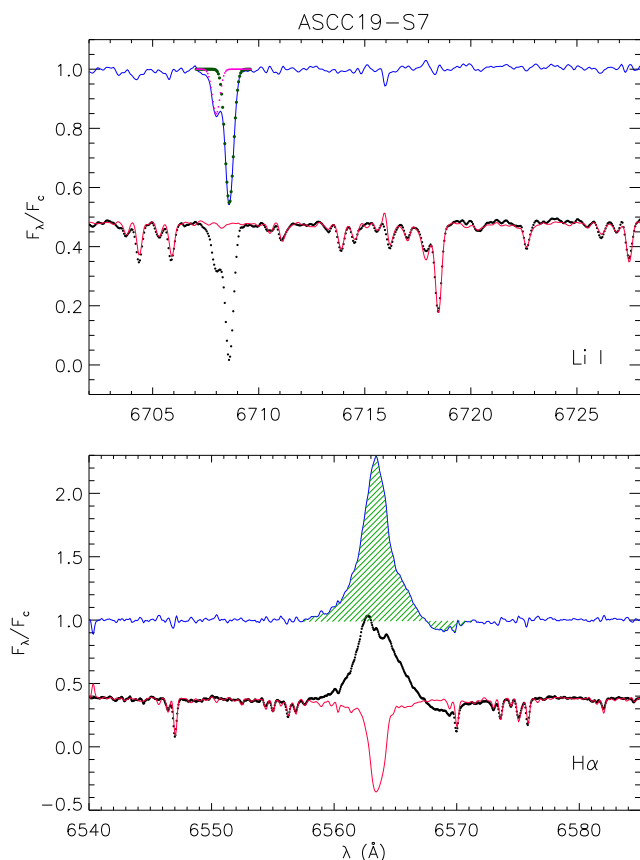


Fig. 4. Subtraction of the synthetic composite spectrum (red line) from the observed spectrum of the SB2 ASCC19-S7 (black dots). The difference washes up the photospheric absorption lines leaving only the chromospheric H α emission (blue line in the *bottom panel*) and emphasizes the Li I λ 6708 Å absorption lines of the two components (blue line in the *top panel*). The green and magenta dotted lines superimposed on the residual spectrum represent Gaussian fits used to deblend the Li I lines of the two components. The two components cannot be resolved in the strong and broad H α emission profile (also showing some redshifted extra-absorption), which has been integrated to provide a total $W_{\text{H}\alpha}^{\text{em}}$ (green hatched area in the *bottom panel*).

deed severely affected by NLTE and redistribution effects that make low-activity standard stars preferable as photospheric templates to be subtracted. Since the signal-to-noise ratio of HARPS-N spectra of our targets is normally quite low in the Ca II H & K region ($S/N \leq 20$), we have degraded the original resolution ($R=115,000$) of the HARPS-N spectra and the synthetic spectra to $R=42,000$, which is the same of the ELODIE templates, improving the S/N but still keeping a resolution sufficient to identify the emission cores and measure their equivalent widths and fluxes. Furthermore, the photospheric templates have been aligned in wavelength with the target spectra by means of the cross-correlation function and have been rotationally broadened by the convolution with a rotational profile with the $v \sin i$ of the target star that is reported in Table 3. The observed spectra (black lines) and the photospheric templates (red lines) are displayed in Fig. A.9 for the Ca II H & K region.

The equivalent width of an emission chromospheric line, such as the H α and Ca II lines of our targets after the sub-

traction of the photospheric spectrum, is not the best diagnostic of the activity level, because it measures the intensity of the line with respect to the local continuum. More effective indicators of activity for a chromospheric line are the surface flux, F_{line} , and the ratio of line luminosity to bolometric luminosity, R'_{line} . For the H α this reads as

$$F_{\text{H}\alpha} = F_{6563} EW_{\text{H}\alpha}, \quad (1)$$

$$R'_{\text{H}\alpha} = L_{\text{H}\alpha}/L_{\text{bol}} = F_{\text{H}\alpha}/(\sigma T_{\text{eff}}^4), \quad (2)$$

where F_{6563} is the flux at the continuum near the H α line per unit stellar surface area, which is evaluated from the BTSettl spectra (Allard et al. 2012) at the stellar temperature and surface gravity of the target. The flux error includes both the error of $W_{\text{H}\alpha}^{\text{em}}$ and the uncertainty in the continuum flux at the line centre, which is estimated propagating the errors of T_{eff} and $\log g$. Similar relations were used for the Ca II H and K lines.

The indexes $R'_{\text{H}\alpha}$ and R'_{HK} are plotted against T_{eff} in Fig. 5 along with the data for the Pleiades stars from Soderblom et al. (1993). The chromospheric emission of the members of the young clusters investigated in the present paper is comparable with that of the Pleiades stars and roughly follows the increasing trend with the decrease of temperature, with two outliers, ASCC19-S16 and ASCC19-S7. The former source is an F2 YSO, a likely Herbig star, whose H α emission is more likely related to magnetospheric accretion. The latter source is an SB2 with a strong and broad H α emission profile where the two components cannot be distinguished, so that it has been fully integrated providing a total flux that has been referred to the primary component. It is likely that the spin-orbit coupling and other effects related to the binary nature are responsible for this high flux.

5. Discussion

5.1. Literature

We searched the literature for spectroscopic studies conducted at high resolution with which compare our results, but we did not find many references. The best one was the study performed by Myers et al. (2022) in the framework of the OCCAM survey. They investigated the chemical composition of 150 OCs based on the analysis of the abundances reported in the APOGEE DR17 ($R=22\,500$). Six out of the seven clusters studied in this work (all except Roslund 6) were also observed by APOGEE, with which we have 15 chemical elements in common. When comparing both sets of abundances, we find that ours are, on average, 0.15 dex higher, with C being the only element that shows a clear different value. As stated in the APOGEE website⁴, the "solar scale should be close to the Grevesse et al. (2007) solar values", which are the ones used as reference by us. However, they do not report these abundances, so that we cannot to put the two data sets on exactly the same scale. This could lead to the existence of offsets between their and our data that could mitigate the observed differences. Figure 6 displays the comparison of the average chemical composition for each element. In addition, for the youngest clusters in

⁴ <https://www.sdss4.org/dr17/irspec/abundances/>

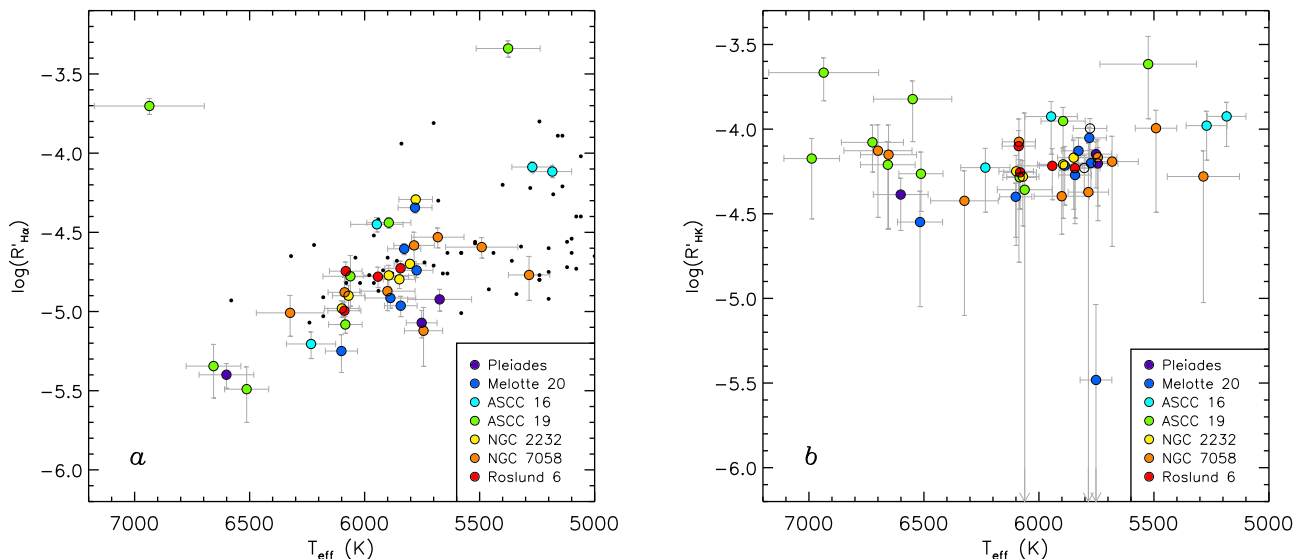


Fig. 5. *a*) The index $R'_{H\alpha}$ as a function of T_{eff} for the members of the seven clusters (big dots) distinguished by the colors. The small black dots denote the measures made by Soderblom et al. (1993) for Pleiades stars. *b*) The index R'_{HK} as a function of T_{eff} .

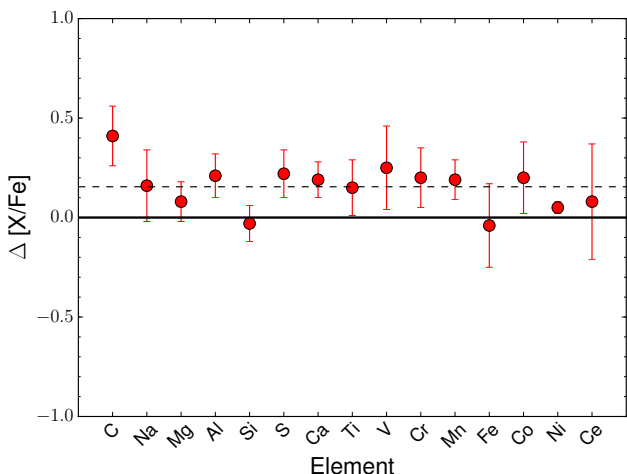


Fig. 6. Differences (ours minus theirs) in the average chemical composition derived in this work and those from APOGEE. The dashed line represents the average offset found between both data sets.

our sample the APOGEE results might be unreliable, as its pipeline does not work optimally with stars younger than about 50 Myr (Kounkel et al. 2018; Myers et al. 2022).

Below we discuss the papers focused on individual clusters, where possible. As previously commented, most of our targets are poorly studied, at least from a chemical point of view, and beyond the paper of Myers et al. (2022) there are not additional references.

5.1.1. NGC 2232

Monroe & Pilachowski (2010) observed this cluster by using the multi-object spectrograph Hydra ($R=16\,000$) mounted on the 3.5-m WIYN telescope, finding a supersolar metal-

licity, $[\text{Fe}/\text{H}]=-0.49\pm 0.09$. They also derived the abundances of Al, Si and Ni, obtaining subsolar $[\text{X}/\text{Fe}]$ ratios for all of them: -0.37 , -0.33 and -0.26 , respectively. In that work, the authors calculated the T_{eff} in two different ways (applying a photometric relationship and fitting the spectral energy distribution), obtaining different abundances as well. The values quoted here are the average of both data sets. Our results differ strongly from theirs: we find a mild subsolar metallicity ($[\text{Fe}/\text{H}]=-0.10$), solar ratios for Si (0.00) and Ni (0.02) and a slight supersolar value for Al (0.18). The cause of this disagreement is certainly due to the different methodology used and is very likely the result of the adoption of photometric temperatures by Monroe & Pilachowski (2010). In any case we consider our results as more reliable, since we used a much higher resolution than them and our findings show a much better agreement with the Galactic gradient and trends (see e.g. Magrini et al. 2023).

As for metallicity, in addition to Monroe & Pilachowski (2010), we also found two other references. Randich et al. (2022), in the GES framework⁵, gave a solar estimate, $[\text{Fe}/\text{H}]=0.02\pm 0.05$ while the above mentioned paper by Myers et al. (2022) found a subsolar value, $[\text{Fe}/\text{H}]=-0.35\pm 0.03$. Despite using high resolution, the metallicity obtained in these four works shows a large spread, of almost one dex, which is striking and calls for further studies.

5.1.2. Pleiades

Gebran & Monier (2008) studied the chemical composition of the Pleiades by observing 16 A-type dwarfs⁶ with ELODIE ($R=42\,000$) and five F-type MS stars with SO-

⁵ NGC 2232 was included in the *Gaia*-ESO Survey, but most of its members were only observed with GIRAFFE at intermediate resolution, and no chemical abundances beyond the metallicity were derived.

⁶ Two of them were discovered to be chemically peculiar and will be not considered in the subsequent discussion.

PHIE ($R=75\,000$). Among their A dwarfs we found two stars that we also observed in this work, namely S7 and S8. For these objects we do not provide abundances since they are too hot for our method. However, the atmospheric parameters estimated in the present work are fully compatible with those reported by Gebran & Monier (2008). As regards the chemical analysis, our results and theirs are compatible within the errors for most of the 17 elements in common, especially in the case of the F stars. They are more similar to our targets and, unlike the sample of A stars, they exhibit a smaller scatter in their chemical composition. Only the abundances of Si, V, and Ba show a clear discrepancy in both works. In the case of V and Ba the values provided by them are too high to be reliable (≈ 1 dex). However, for Si the explanation is not evident. For this element, they reported a supersolar value around $+0.25$ dex while we found a slightly subsolar abundance (≈ -0.1 dex).

In order to determine the cluster metallicity with a great accuracy Soderblom et al. (2009) conducted some observations from the Lick Observatory. They used the Hamilton echelle spectrograph ($R=40\,000$) to obtain spectra of 20 FGK stars, out of which 17 are bona fide members according to Cantat-Gaudin et al. (2020). They found a solar metallicity for the Pleiades ($[\text{Fe}/\text{H}]=0.03\pm 0.02$), the same value derived in this paper, in good agreement with previous works. They also calculated the chemical abundances of Na, Si, Ti and Ni, whose values are again consistent with our results.

Recently, Spina et al. (2018) examined the chemical inhomogeneities in the Pleiades from five solar-like stars (none of them in common with us). They used UVES spectra ($R=75\,000$) to derive chemical abundances for 19 elements, all of which were also investigated in this work with the exception of oxygen. They performed a line-by-line differential analysis relative to the solar spectrum, a procedure somewhat different than ours that precludes a direct comparison of both sets of results. In any case, for most elements, the abundances derived in this work agree very well with those of Spina et al. (2018). Only for C, Al, Si and Co the differences are slightly greater than 0.2 dex.

5.2. Galactic metallicity gradient

As done in previous papers, we compare the metallicities found in this work for our targets with those expected based on their position in the Galaxy. We used a large sample of OCs to trace the radial metallicity distribution of the Galaxy to which we contrast our results. We only collected OCs studied with high-resolution spectroscopy in the framework of surveys such as OCCAM (APOGEE-DR17, Myers et al. 2022), GES (iDR6, Randich et al. 2022), OC-CASO (Carbajo-Hijarrubia et al. 2024), and SPA (Frasca et al. 2019; D’Orazi et al. 2020; Casali et al. 2020; Zhang et al. 2021; Alonso-Santiago et al. 2021). We completed the sample with other clusters studied previously by our group (Alonso-Santiago et al. 2017, 2018, 2019, 2020, 2024) in a similar way. In total, we gathered nearly two hundreds OCs, at Galactocentric distances (R_{GC}) up to 16 kpc. Only a few of them were common in different datasets. With all these clusters we plot the Galactic gradient shown in Fig. 7. We used the Grevesse et al. (2007) solar value, $A(\text{Fe})=7.45$, to rescale the metallicities and took the values reported in Cantat-Gaudin et al. (2020) for the R_{GC} . These were calcu-

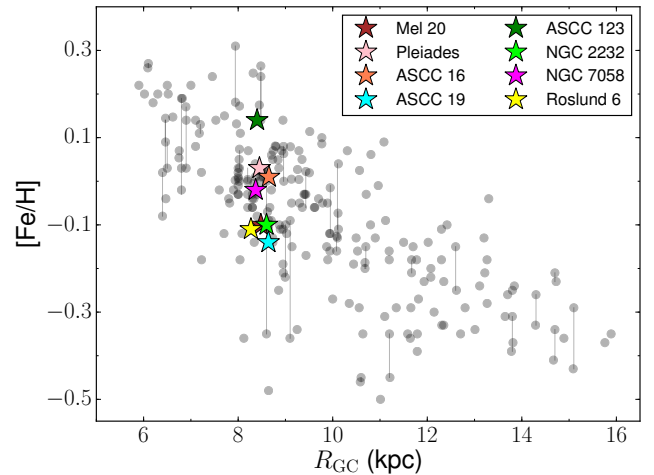


Fig. 7. Radial metallicity gradient traced by literature open clusters observed at high resolution (grey circles). Vertical lines link different results for the same cluster. The objects studied in this work are highlighted with different colours.

lated from the analysis of the *Gaia*-DR2 astrometry, using $R_{\odot}=8.34$ kpc as a solar reference.

Our targets are located in the vicinity of the Sun at similar distances ($R_{GC} \approx 8.6$ kpc). However, as discussed before, they show a spread of about 0.2 dex in metallicity, which increases up to ≈ 0.3 dex when ASCC 123 is also considered. In Sect.6 we will explore its possible age dependence. In any case, as seen in Fig. 7, their positions on the gradient are totally compatible with those of the rest of the clusters. In the figure is also visible the well-known fact that the $[\text{Fe}/\text{H}]$ obtained at high resolution by different groups for the same objects differ by 0.1–0.2 dex, similar to the dispersion observed in our clusters.

5.3. Chemical composition and Galactic trends

In an analogous way to that previously carried out with metallicity, we compare the abundances found in this work with those observed in the Galactic disc. To this aim we used the chemical trends displayed by the OCs collected in the sample described in Sect. 5.2. Additionally, we increased the number of chemical elements investigated in the GES and SPA clusters by considering the new abundances reported in Magrini et al. (2023) and Zhang et al. (2022), respectively.

Figure 8 shows the Galactic trends, represented by the ratios $[X/\text{Fe}]$ versus $[\text{Fe}/\text{H}]$, for 23 chemical elements. With the only exception of C, the chemical composition of the clusters under study is fully compatible with the observed trends. Zinc is the only element for which our clusters show a slightly subsolar value, but close to the trend. The opposite happens with S, for which our abundances lie above the gradient, but compatible within the errors (not shown in the figure for clarity). Barium is the element that shows the largest spread among the clusters.

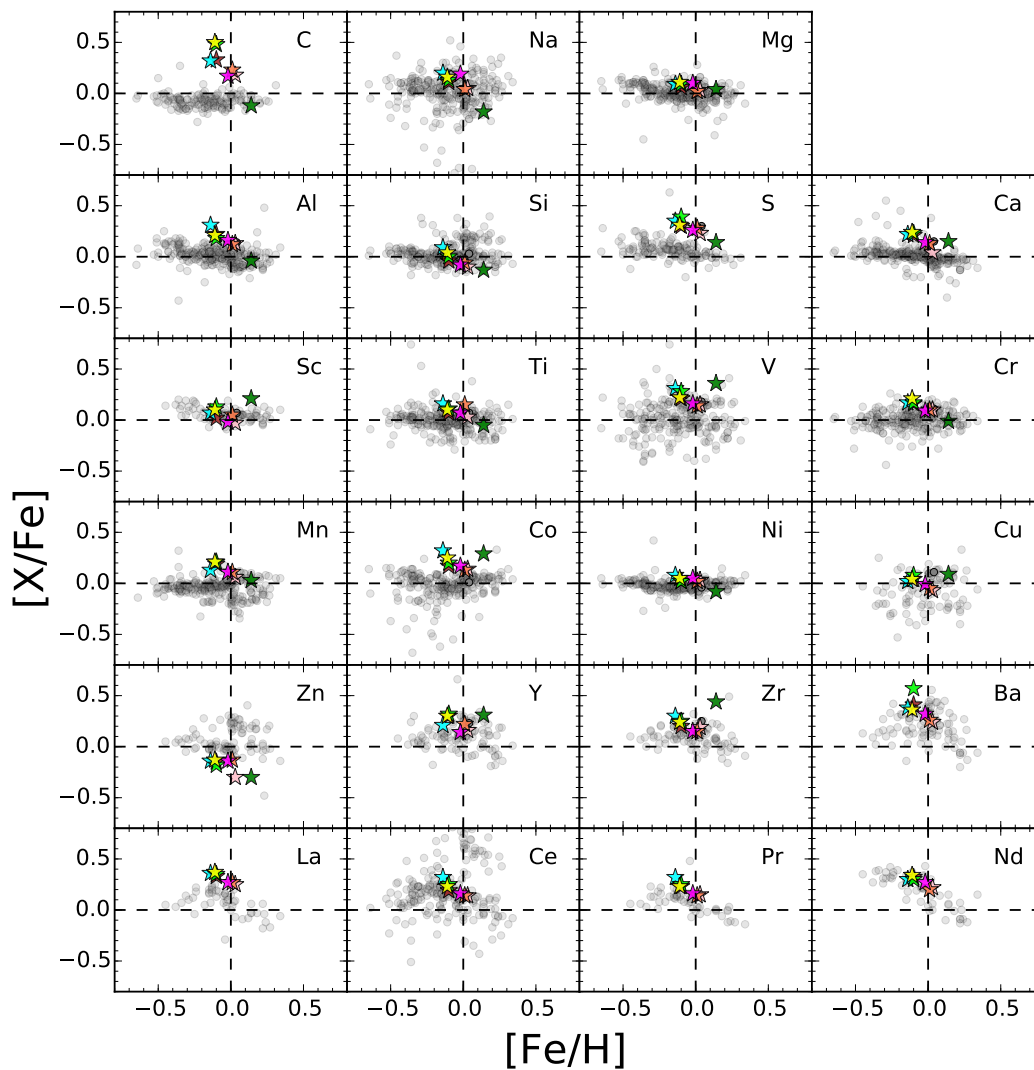


Fig. 8. Abundance ratios $[X/Fe]$ vs. $[Fe/H]$. Symbols and colors are the same as in Fig. 7. The dashed lines show the solar value.

6. The Radcliffe Wave

In order to investigate the possible connection among the Radcliffe clusters we studied the correlation between the different variables that we have at our disposal: chemical composition, age, and position in the Galaxy. In each of these three groups we included several data sets: R_{GC} , Cartesian Galactic coordinates (X , Y , Z), age, $[Fe/H]$, $[X/H]$, and $[X/Fe]$ from the present research and the literature (Cantat-Gaudin et al. 2020; Myers et al. 2022; Hunt & Reffert 2023; Cavallo et al. 2024). Figure 9 illustrates the distribution of our targets along the RW according to the age and metallicity obtained in this work for them.

The degree of correlation, expressed by the Pearson’s coefficient, varies according to the data sets we use. For example, we find a moderate-to-high correlation ($0.65 < |r| < 0.94$) between age and Galactic position when using the values derived in this work or in Cantat-Gaudin et al. (2020). On the contrary, no significant correlation is found using the ages reported in Hunt & Reffert (2023) and Cavallo et al. (2024). Metallicity shows the strongest correlation with age ($r \approx 0.8$) when combining the metallicity obtained

in this work (the value derived with ROTFIT correlates slightly better than that of SYNTHE) and the ages of both Hunt & Reffert (2023) and Cavallo et al. (2024).

Concerning the chemical composition, we find a strong correlation with age (taking as a reference the values from Hunt & Reffert (2023) and Cavallo et al. (2024)) of α - ($r=0.78$), Fe-peak ($r=0.93$) and neutron-capture ($r = 0.98$) elements in terms of $[X/H]$ abundances. On the other hand, if we use the $[X/Fe]$ ratios, the correlation of α - ($r=-0.64$) and neutron-capture ($r = 0.56$) elements drops and that of the Fe-peak elements disappears. As far as individual chemical elements are concerned, a correlation of at least moderate magnitude is observed for many of them. In particular, employing the $[X/H]$ values, we find a moderate correlation ($0.6 < |r| < 0.8$) for C, Na, Al, Mn, and Nd and a strong correlation ($|r| > 0.8$) for Mg, Ca, Sc, V, Co, Cu, Y, and Zr. When the $[X/Fe]$ values are used instead, the correlation is moderate for C, S, Sc, Cr, and Zn while it is strong for Na, Al, Ti, Ni, and Zr. By contrast, no correlation is found when using the ages derived in the present work or those reported in Cantat-Gaudin et al. (2020).

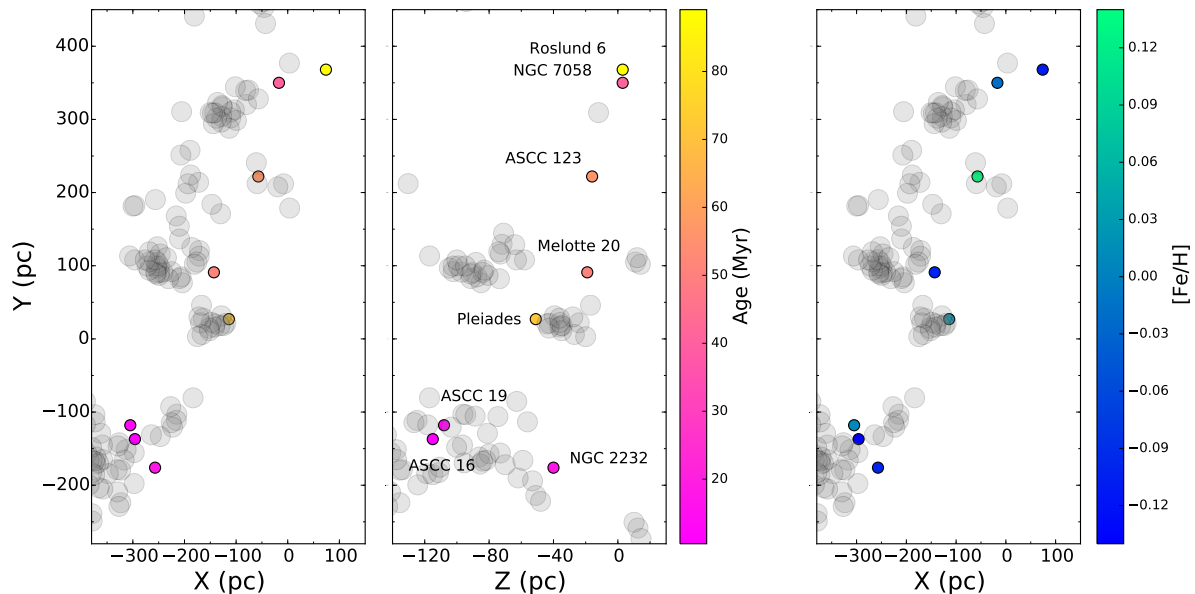


Fig. 9. Distribution of the molecular clouds forming the Radcliffe Wave in the XY and ZY planes (grey circles). Our targets are represented with different colors depending on their age (left) and metallicity (right).

Finally, we also used the chemical abundances ($[X/Fe]$) calculated by Myers et al. (2022). As commented before, Roslund 6 and ASCC 123 were not included in their sample. They derived the abundances for the same α elements investigated by us, some Fe-peak elements (Cr, Mn, Co, Ni and Cu) and Ce as the only heavy element. Their data correlate best with those of Hunt & Reffert (2023). The dependence of $[Fe/H]$ on age is somewhat stronger than ours, while for α - and Fe-peak elements are similar. For the latter, on the contrary, the correlation is positive. Regarding the spatial distribution, the correlation of $[Fe/H]$ with R_{GC} is slightly higher than ours, while no correlation for chemical abundances is found. Concerning the X, Y, Z coordinates a moderate level of correlation, somewhat stronger than ours, is found. No clear trend ($|r| > 0.6$) is evident between chemical abundances and age or Galactic location.

However, if we group the clusters by age, the correlation becomes very clear with all data sets. In this way we considered three categories. The first contained the youngest clusters of our sample: ASCC 16, ASCC 19 and NGC 2232. The second group consisted of the clusters with "intermediate" age, Melotte 20 and NGC 7058, while the third group contained the oldest cluster, Roslund 6. The classification of the two remaining clusters, ASCC 123 and Pleiades, depends on the set of ages we use. Based on the ages of Hunt & Reffert (2023) and Cavallo et al. (2024) they should be included in the last category, whereas if we consider the ages of this work both clusters should be classified as intermediate-age clusters. Finally, according to the values of Cantat-Gaudin et al. (2020), ASCC 123 would be included in the second group and the Pleiades in the third.

Furthermore, to try to evaluate the significance of their position along the RW, instead of using individual coordinates as done before, we payed attention to their location in the planes XY, XZ and YZ. In this way we used the sum of the pair of coordinates that defines each plane, as a

marker of the position of the cluster on it, that is, $X+Y$ in the case of the XY plane. We find an age gradient across the RW, with older clusters close to the Galactic centre (e.g. $0.8 < r < 0.9$ in all the three planes when using the data reported in Cantat-Gaudin et al. 2020). This fact confirms the main conclusion of Konietzka et al. (2024), namely the existence of a radial oscillation in the RW from the Galactic centre outwards. On the other hand, the Pearson's coefficients between the metallicity and chemical composition derived in this work and age or position in the Wave according to Hunt & Reffert (2023) and Cantat-Gaudin et al. (2020), respectively, range from ≈ 0.8 to 1.0 and are listed in Table 9. As an example, some of these correlations are displayed in Fig. 10, specifically the variation of metallicity and chemical content derived in this work with respect to age and location in the XY plane reported in Cavallo et al. (2024). Correlations are slightly stronger when $[X/Fe]$ is used instead of $[X/H]$, Similar values are obtained when we used the APOGEE abundances or other ages as ours or those of Hunt & Reffert (2023). The only difference we noted is the behaviour of the Fe-peak elements (but not $[Fe/H]$ or α elements): we find negative correlations between $[X/Fe]$ and age or XYZ positions, while when considering the APOGEE abundances the correlation is positive.

From our results we infer a slight variation in the chemical composition with age and the position along the Wave, which is the first evidence of the connection between the different clusters associated to the RW. The observed metallicity trend, with younger clusters being metal-poorer compared to older ones, suggests inhomogeneous mixing or local chemical enrichment rather than a canonical triggered star formation within a large-star forming region. Additionally, it is important to note, especially in the youngest stars, the effect that strong magnetic fields can induce on the behaviour of spectral features, which could potentially alter the analysis and, therefore, the results (Baratella et al.

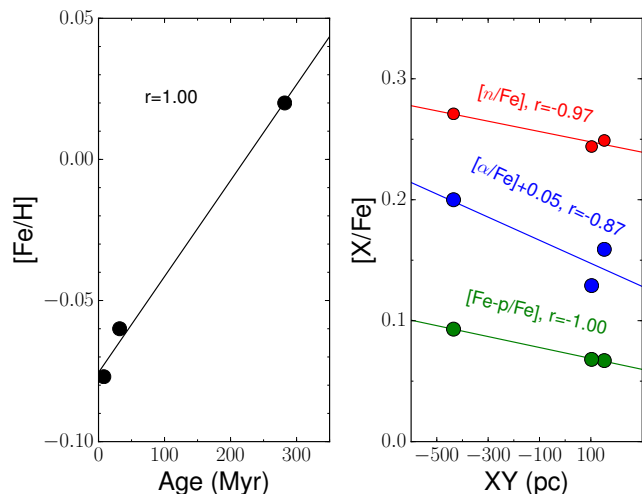


Fig. 10. Some of the correlations found in the Radcliffe clusters, grouped into age bins. Left panel: evolution of $[\text{Fe}/\text{H}]$ over time. Right panel: distribution of chemical composition, $[\text{X}/\text{Fe}]$, along the XZ Galactic plane. The Pearson coefficients (r) are also shown.

2021). In any case the sample of clusters is not very large and these results have been obtained from the analysis of six to eight points (when considering the clusters separately) or only three (when we grouped them into age bins).

7. Summary

The Radcliffe Wave is a ≈ 3 kpc structure in the solar neighbourhood that involves many of the nearby star-forming regions. Recently discovered, it has superseded the Gould Belt as the preferred scenario for the local star formation. In this work, for the first time, the RW is studied also from a chemical point of view with the idea of finding traces of metal content evolution throughout its history. To conduct our research we selected a sample of seven young OCs associated to the Wave namely, Melotte 20, Pleiades, NGC 2232, NGC 7058, ASCC 16, ASCC 19 and Roslund 6 (and added ASCC 123, previously studied by our group). Their age range varies from around 10 to 100, Myr and most of them are poorly studied. We present here the most complete chemical study to date of these clusters. In the case of Roslund 6, it is also the only one.

We took high-resolution spectra with GIARPS at the TNG telescope of 53 bona fide clusters members, for which we derived radial velocities and atmospheric parameters. Most of the stars observed, 41, are slowly-rotating FGK dwarfs. For this subsample we studied the chromospheric activity and the content of Li, from which we estimated the age of the clusters. The chromospheric activity intensity traced by both the $\text{H}\alpha$ and Ca II H\&K line fluxes is consistent with the young age of these stars, but the data do not allow us to distinguish different levels or trends between the seven clusters. We find that the Li-depletion ages derived in this work agree well with the evolutionary ages reported in the literature. We find that three of the studied clusters have solar metallicity (Pleiades, ASCC 16 and NGC 7058) while the remaining ones (ASCC 19, Melotte 20, NGC 2232 and NGC 7058) show a slightly subsolar value,

around -0.1 dex. In any case, all of them follow the Galactic gradient shown by other OCs.

In addition, we investigated their chemical composition by deriving the abundances of 25 elements, which include the main nucleosynthesis channels. Specifically we determined the chemical abundances of C, odd-Z elements (Na, Al), α -elements (Mg, Si, S, Ca, Ti), Fe-peak elements (Sc, V, Cr, Mn, Co, Ni, Cu, Zn) and neutron-capture elements (Sr, Y, Zr, Ba, La, Ce, Pr, Nd). We find, on average, solar values for α - and Fe-peak elements while the heaviest elements exhibit abundances ≈ 0.2 dex higher, specially barium. Their $[\text{X}/\text{Fe}]$ ratios are in good agreement with the Galactic trends displayed by a large sample of OCs observed at high-resolution. The abundances of C and S are slightly above these trends whereas that of Zn is just below, but in both cases, they are compatible within the errors.

Finally, we investigated the possible link between these clusters as members of the RW. In our analysis we also included ASCC 123, another cluster connected to the RW that was previously studied by our group with the same instrument and methodology. We calculated the Pearson correlation coefficients for different variables (age, XYZ Galactic coordinates, R_{GC} , $[\text{Fe}/\text{H}]$ and chemical abundances) collected from both this work and literature. We find a strong correlation between the age of the clusters and their spatial distribution confirming the radial oscillation along the RW, but no clear correlation between the chemical composition of the clusters and their age or position along the Wave emerges. However, if we do not consider individually the eight clusters, but we group them in three age classes, the correlation becomes very evident. The dependence between metallicity and chemical composition with age and position along the Radcliffe Wave supports the idea of a shared history between our targets, whose palpable result is the local enrichment found, within an episode of inhomogeneous mixing. However, our sample is not very large and prevents us from going further in our conclusions. More data, such as those which will emerge from upcoming large spectroscopic surveys as WEAVE and 4MOST, are needed to confirm the first evidence claimed in this work.

Acknowledgements. We thank the referee, Dr. V.V. Bobylev, for his helpful comments and suggestions. We also acknowledge the INAF support under GO project No. 1.05.23.05.19. This research used the facilities of the Italian Center for Astronomical Archive (IA2) operated by INAF at the Astronomical Observatory of Trieste. This research has made use of the VizieR catalogue access tool, CDS, Strasbourg, France (Ochsenbein 1996). The original description of the VizieR service was published in Ochsenbein et al. (2000). This work has made use of data from the European Space Agency (ESA) mission *Gaia* (<https://www.cosmos.esa.int/gaia>), processed by the *Gaia* Data Processing and Analysis Consortium (DPAC, <https://www.cosmos.esa.int/web/gaia/dpac/consortium>). Funding for the DPAC has been provided by national institutions, in particular the institutions participating in the *Gaia* Multilateral Agreement. We made use of data from the GES Data Archive, prepared and hosted by the Wide Field Astronomy Unit, Institute for Astronomy, University of Edinburgh, which is funded by the UK Science and Technology Facilities Council. This paper includes data collected by the *TESS* mission which are publicly available from the Mikulski Archive for Space Telescopes (MAST). Funding for the *TESS* mission is provided by the NASA's Science Mission Directorate. AF acknowledges funding from the Large-Grant INAF YODA (YSOs Outflow, Disks and Accretion). AB acknowledges funding from INAF Mini-Grant 2022. XF thanks the support of the National Natural Science Foundation of China (NSFC) No. 12203100 and the China Manned Space Project with No. CMS-CSST-2021-A08.

References

- Alfaro, E. J., Jiménez, M., Sánchez-Gil, M. C., et al. 2022, *ApJ*, 937, 114
- Allard, F., Homeier, D., & Freytag, B. 2012, *Philosophical Transactions of the Royal Society of London Series A*, 370, 2765
- Alonso-Santiago, J., Frasca, A., Catanzaro, G., et al. 2021, *A&A*, 656, A149
- Alonso-Santiago, J., Frasca, A., Catanzaro, G., et al. 2024, *A&A*, 683, A75
- Alonso-Santiago, J., Marco, A., Negueruela, I., et al. 2018, *A&A*, 616, A124
- Alonso-Santiago, J., Negueruela, I., Marco, A., Taberero, H. M., & Castro, N. 2020, *A&A*, 644, A136
- Alonso-Santiago, J., Negueruela, I., Marco, A., et al. 2017, *MNRAS*, 469, 1330
- Alonso-Santiago, J., Negueruela, I., Marco, A., et al. 2019, *A&A*, 631, A124
- Alves, J., Zucker, C., Goodman, A. A., et al. 2020, *Nature*, 578, 237
- Antoja, T., Helmi, A., Romero-Gómez, M., et al. 2018, *Nature*, 561, 360
- Armillotta, L., Krumholz, M. R., & Fujimoto, Y. 2018, *MNRAS*, 481, 5000
- Baranne, A., Queloz, D., Mayor, M., et al. 1996, *A&AS*, 119, 373
- Baratella, M., D’Orazi, V., Sheminova, V., et al. 2021, *A&A*, 653, A67
- Barnes, S. A. 2003, *ApJ*, 586, 464
- Bevington, P. R. & Robinson, D. K. 2003, *Data reduction and error analysis for the physical sciences*
- Binks, A. S., Jeffries, R. D., Jackson, R. J., et al. 2021, *MNRAS*, 505, 1280
- Bobylev, V. V. & Bajkova, A. T. 2024, *Research in Astronomy and Astrophysics*, 24, 035010
- Bobylev, V. V., Bajkova, A. T., & Mishurov, Y. N. 2022, *Astronomy Letters*, 48, 434
- Cantat-Gaudin, T., Anders, F., Castro-Ginard, A., et al. 2020, *A&A*, 640, A1
- Carbajo-Hijarrubia, J., Casamiquela, L., Carrera, R., et al. 2024, *A&A*, 687, A239
- Casali, G., Magrini, L., Frasca, A., et al. 2020, *A&A*, 643, A12
- Castelli, F. & Hubrig, S. 2004, *A&A*, 425, 263
- Castro-Ginard, A., Jordi, C., Luri, X., et al. 2020, *A&A*, 635, A45
- Castro-Ginard, A., Jordi, C., Luri, X., et al. 2022, *A&A*, 661, A118
- Catanzaro, G., Frasca, A., Alonso-Santiago, J., & Colombo, C. 2024, *arXiv e-prints*, arXiv:2402.16648
- Catanzaro, G., Ripepi, V., Bernabei, S., et al. 2011, *MNRAS*, 411, 1167
- Catanzaro, G., Ripepi, V., & Bruntt, H. 2013, *MNRAS*, 431, 3258
- Cavallo, L., Spina, L., Carraro, G., et al. 2024, *AJ*, 167, 12
- Claudi, R., Benatti, S., Carleo, I., et al. 2017, *European Physical Journal Plus*, 132, 364
- Cosentino, R., Lovis, C., Pepe, F., et al. 2014, in *Society of Photo-Optical Instrumentation Engineers (SPIE) Conference Series*, Vol. 9147, *Ground-based and Airborne Instrumentation for Astronomy V*, ed. S. K. Ramsay, I. S. McLean, & H. Takami, 91478C
- De Cia, A., Jenkins, E. B., Fox, A. J., et al. 2021, *Nature*, 597, 206
- Deason, A. J. & Belokurov, V. 2024, *arXiv e-prints*, arXiv:2402.12443
- Dias, W. S., Monteiro, H., Moitinho, A., et al. 2021, *MNRAS*, 504, 356
- Donada, J. & Figueras, F. 2021, *arXiv e-prints*, arXiv:2111.04685
- D’Orazi, V., Oliva, E., Bragaglia, A., et al. 2020, *A&A*, 633, A38
- Fleck, R. 2020, *Nature*, 583, E24
- Frasca, A., Alonso-Santiago, J., Catanzaro, G., & Bragaglia, A. 2023a, *MNRAS*, 522, 4894
- Frasca, A., Alonso-Santiago, J., Catanzaro, G., et al. 2019, *A&A*, 632, A16
- Frasca, A., Alonso-Santiago, J., Catanzaro, G., et al. 2023b, *A&A*, 677, A154
- Frasca, A., Biazzo, K., Alcalá, J. M., et al. 2017, *A&A*, 602, A33
- Frasca, A., Biazzo, K., Kóvári, Z., Marilli, E., & Çakırlı, Ö. 2010, *A&A*, 518, A48
- Frasca, A., Biazzo, K., Lanzafame, A. C., et al. 2015, *A&A*, 575, A4
- Frasca, A., Freire Ferrero, R., Marilli, E., & Catalano, S. 2000, *A&A*, 364, 179
- Frasca, A., Fröhlich, H. E., Bonanno, A., et al. 2011, *A&A*, 532, A81
- Frasca, A., Guillout, P., Marilli, E., et al. 2006, *A&A*, 454, 301
- Frasca, A., Montes, D., Alcalá, J. M., Klutsch, A., & Guillout, P. 2018, *Acta Astron.*, 68, 403
- Frémat, Y., Royer, F., Marchal, O., et al. 2023, *A&A*, 674, A8
- Fritzewski, D. J., Barnes, S. A., James, D. J., & Strassmeier, K. G. 2020, *A&A*, 641, A51
- Fu, X., Bragaglia, A., Liu, C., et al. 2022, *A&A*, 668, A4
- Gaia Collaboration, Prusti, T., de Bruijne, J. H. J., et al. 2016, *A&A*, 595, A1
- Gaia Collaboration, Vallenari, A., Brown, A. G. A., et al. 2023, *A&A*, 674, A1
- Gebran, M. & Monier, R. 2008, *A&A*, 483, 567
- Gould, B. A. 1874, *American Journal of Science and Arts*, 8, 325
- Green, G. M., Schlafly, E., Zucker, C., Speagle, J. S., & Finkbeiner, D. 2019, *ApJ*, 887, 93
- Grevesse, N., Asplund, M., & Sauval, A. J. 2007, *Space Sci. Rev.*, 130, 105
- Guillout, P., Sterzik, M. F., Schmitt, J. H. M. M., Motch, C., & Neuhaeuser, R. 1998, *A&A*, 337, 113
- Helmi, A., Babusiaux, C., Koppelman, H. H., et al. 2018, *Nature*, 563, 85
- Hunt, E. L. & Reffert, S. 2023, *A&A*, 673, A114
- Jeffries, R. D. 2014, in *EAS Publications Series*, Vol. 65, *EAS Publications Series*, ed. Y. Lebreton, D. Valls-Gabaud, & C. Charbonnel, 289–325
- Jeffries, R. D., Jackson, R. J., Wright, N. J., et al. 2023, *MNRAS*, 523, 802
- Konietzka, R., Goodman, A. A., Zucker, C., et al. 2024, *Nature*, 628, 62
- Kounkel, M. & Covey, K. 2019, *AJ*, 158, 122
- Kounkel, M., Covey, K., & Stassun, K. G. 2020, *AJ*, 160, 279
- Kounkel, M., Covey, K., Suárez, G., et al. 2018, *AJ*, 156, 84
- Kurucz, R. 1993a, *ATLAS9 Stellar Atmosphere Programs and 2 km/s grid*. Kurucz CD-ROM No. 13. Cambridge, 13
- Kurucz, R. L. 1993b, in *Astronomical Society of the Pacific Conference Series*, Vol. 44, *IAU Colloq. 138: Peculiar versus Normal Phenomena in A-type and Related Stars*, ed. M. M. Dworetzky, F. Castelli, & R. Faraggiana, 87
- Kurucz, R. L. & Avrett, E. H. 1981, *SAO Special Report*, 391
- Kurucz, R. L. & Bell, B. 1995, *Atomic line list*
- Lallement, R., Babusiaux, C., Vergely, J. L., et al. 2019, *A&A*, 625, A135
- Li, G.-X. & Chen, B.-Q. 2022, *MNRAS*, 517, L102
- Lind, K., Asplund, M., & Barklem, P. S. 2009, *A&A*, 503, 541
- Magrini, L., Viscasillas Vázquez, C., Spina, L., et al. 2023, *A&A*, 669, A119
- Mermilliod, J. C., Rosvick, J. M., Duquennoy, A., & Mayor, M. 1992, *A&A*, 265, 513
- Monroe, T. R. & Pilachowski, C. A. 2010, *AJ*, 140, 2109
- Myers, N., Donor, J., Spoo, T., et al. 2022, *AJ*, 164, 85
- Ochsenbein, F. 1996, *The VizieR database of astronomical catalogues*
- Ochsenbein, F., Bauer, P., & Marcout, J. 2000, *A&AS*, 143, 23
- Oliva, E., Origlia, L., Maiolino, R., et al. 2012, in *Society of Photo-Optical Instrumentation Engineers (SPIE) Conference Series*, Vol. 8446, *Ground-based and Airborne Instrumentation for Astronomy IV*, ed. I. S. McLean, S. K. Ramsay, & H. Takami, 84463T
- Origlia, L., Oliva, E., Baffa, C., et al. 2014, in *Society of Photo-Optical Instrumentation Engineers (SPIE) Conference Series*, Vol. 9147, *Ground-based and Airborne Instrumentation for Astronomy V*, ed. S. K. Ramsay, I. S. McLean, & H. Takami, 91471E
- Palouš, J. & Ehlerová, S. 2017, in *Handbook of Supernovae*, ed. A. W. Alsabti & P. Murdin, 2301
- Pepe, F., Mayor, M., Galland, F., et al. 2002, *A&A*, 388, 632
- Randich, S., Gilmore, G., Magrini, L., et al. 2022, *A&A*, 666, A121
- Rebull, L. M., Stauffer, J. R., Bouvier, J., et al. 2016, *AJ*, 152, 113
- Ricker, G. R., Winn, J. N., Vanderspek, R., et al. 2015, *Journal of Astronomical Telescopes, Instruments, and Systems*, 1, 014003
- Roberts, D. H., Lehar, J., & Dreher, J. W. 1987, *AJ*, 93, 968
- Romaniello, M., Primas, F., Mottini, M., et al. 2008, *A&A*, 488, 731
- Scargle, J. D. 1982, *ApJ*, 263, 835
- Smiljanic, R., Korn, A. J., Bergemann, M., et al. 2014, *A&A*, 570, A122
- Soderblom, D. R., Laskar, T., Valenti, J. A., Stauffer, J. R., & Rebull, L. M. 2009, *AJ*, 138, 1292
- Soderblom, D. R., Stauffer, J. R., Hudon, J. D., & Jones, B. F. 1993, *ApJS*, 85, 315
- Spina, L., Meléndez, J., Casey, A. R., Karakas, A. I., & Tucci-Maia, M. 2018, *ApJ*, 863, 179
- Swiggum, C., Alves, J., D’Onghia, E., et al. 2022, *A&A*, 664, L13
- Thulasidharan, L., D’Onghia, E., Poggio, E., et al. 2022, *A&A*, 660, L12
- Torres, G., Latham, D. W., & Quinn, S. N. 2021, *ApJ*, 921, 117
- Tu, A. J., Zucker, C., Speagle, J. S., et al. 2022, *ApJ*, 936, 57
- Zhang, R., Lucatello, S., Bragaglia, A., et al. 2022, *A&A*, 667, A103
- Zhang, R., Lucatello, S., Bragaglia, A., et al. 2021, *A&A*, 654, A77
- Zucker, C., Goodman, A. A., Alves, J., et al. 2022, *Nature*, 601, 334
- Zucker, C., Speagle, J. S., Schlafly, E. F., et al. 2020, *A&A*, 633, A51

Table 7. $\text{Li I } \lambda 6708 \text{ \AA}$ equivalent width and abundance of the cool stars observed in this work.

Star	T_{eff} (K)	EW_{Li} (mÅ)	$A(\text{Li})$
Mel20-A1	5752±69	51±6	2.33±0.10
Mel20-A2	5843±71	153±6	2.96±0.07
Mel20-A3	6101±70	115±5	2.97±0.07
Mel20-S1	5774±71	150±9	2.91±0.09
Mel20-S2	5781±74	181±7	3.03±0.07
Mel20-S3	5888±110	146±6	2.97±0.09
Mel20-S8	5828±72	151±5	2.95±0.06
Mel20-S11A	6119±75	86±5 ^a	2.83±0.08
Mel20-S11B	5172±240	275±37 ^a	2.87±0.29
Plei-S2A	5674±139	174±13 ^a	2.93±0.14
Plei-S2B	5371±172	153±14 ^a	2.63±.19
Plei-S3	6601±119	32±7	2.64±0.18
Plei-S5	5752±67	175±5	2.98±0.06
Plei-S7	7107±12	22±5	...
Plei-S8	7280±269	20±5	...
Plei-S9	7536±308	12±3	...
ASCC16-S1	5271±89	304±9	3.03±0.10
ASCC16-S2	5184±84	325±9	3.02±0.10
ASCC16-S6	5947±114	183±11	3.14±0.11
ASCC16-S12	6233±107	128±7	3.11±0.09
ASCC19-S1	6724±135	108±14	3.30±0.14
ASCC19-S2	6549±170	25±8	2.49±0.25
ASCC19-S3	6657±119	52±24	2.90±0.30
ASCC19-S4	6062±119	176±30	3.19±0.18
ASCC19-S5	6084±73	152±5	3.11±0.07
ASCC19-S6	5895±96	222±7	3.23±0.09
ASCC19-S7A	5376±139	284±10 ^a	3.06±0.14
ASCC19-S7B	4894±226	403±38 ^a	3.04±0.36
ASCC19-S14	6513±96	101±6	3.14±0.09
ASCC19-S15	6988±121	53±11	3.10±0.13
ASCC19-S16	6750±220	63±5	3.15±0.14
NGC2231-A2	5778±73	194±7	3.07±0.07
NGC2231-A3	5803±69	139±6	2.89±0.07
NGC2232-S3	5895±111	155±9	3.01±0.11
NGC2232-S4A	6070±70	116±7 ^a	2.95±0.07
NGC2232-S4B	4130±60	361±81 ^a	1.97±0.35
NGC2232-S9	5849±70	151±10	2.96±0.09
NGC2232-S11	6099±75	123±7	3.01±0.08
Ros6-S1	5942±133	125±5	2.91±0.11
Ros6-S2	6082±71	93±7	2.84±0.08
Ros6-S5	5844±68	117±7	2.82±0.08
Ros6-S9	6088±72	135±7	3.06±0.07
NGC7058-S5	6324±147	62±19	2.79±0.24
NGC7058-S6	6087±72	189±22	3.24±0.11
NGC7058-S7	5901±120	139±15	2.95±0.14
NGC7058-S9	5785±88	88±12	2.63±0.13
NGC7058-S10	5744±83	190±12	3.03±0.10
NGC7058-S11	5682±114	205±10	3.04±0.10
NGC7058-S12	5491±157	202±14	2.90±0.16
NGC7058-S13	5285±90	132±14	2.49±0.13

^a Values corrected for the contribution to the continuum flux.

Table 8. Comparison of the age (Myr) of our targets derived in this work (TW) and literature: Cantat-Gaudin et al. (2020, CG20), Hunt & Reffert (2023, HR23) and Cavallo et al. (2024, C24).

Cluster	TW	CG20	HR23	C24
Melotte 20	68±28	51	56±32	42±9
Pleiades	75±36	78	122±71	87±17
ASCC 16	14±10	14	8±2	5±1
ASCC 19	< 20	11	7±3	6±2
NGC 2232	29±10	18	13±7	12±2
Roslund 6	108±66	89	168±114	98±19
NGC 7058	65±13	41	70±44	21±6
ASCC 123	57±17	45	1064±657	661±157

Table 9. Pearson correlation coefficients between different variables for the Radcliffe clusters grouped by age.

	[Fe/H]	[α /Fe]	[Fe - peak/Fe]	[n/Fe]
Age	1.00	-0.88	-0.88	-0.84
R _{GC}	-0.77	0.97	0.97	1.00
XY	0.81	-0.93	-1.00	-0.97
XZ	0.76	-0.94	-0.99	-0.98
YZ	0.87	-0.88	-0.73	-0.94

Appendix A: Additional tables and figures

Table A.1. *Gaia* DR3 astrometric data and cluster membership.

Star	TIC	RA (J2000)	DEC (J2000)	ϖ (mas)	μ_{α^*} (mas a ⁻¹)	μ_{δ} (mas a ⁻¹)	G^a (mag)	$G_{BP} - G_{RP}^a$ (mag)	V_{broad} (kms ⁻¹)	Prob ^d
Mel20-A1	116991727	047.466998	+48.470950	4.2466 0.0191	19.717 0.020	-24.251 0.018	10.669893	1.001655	5.6594	...
Mel20-A2	117805849	049.709634	+49.731154	5.6468 0.0173	23.170 0.019	-24.502 0.019	10.987741	0.892536	13.0912	1.00
Mel20-A3	410705987	051.979241	+49.760330	5.7952 0.0158	22.636 0.013	-26.262 0.015	10.539244	0.824582	10.8013	1.00
Mel20-S1	431769464	053.574571	+45.730075	5.6585 0.0204	21.186 0.024	-26.255 0.018	11.345673	0.953852	7.5463	1.00
Mel20-S2	252867743	051.580672	+49.225693	5.7431 0.0219	23.253 0.020	-24.705 0.020	11.409828	0.972621	14.8571	1.00
Mel20-S3	458811423	050.264157	+58.507704	5.4226 0.0252	22.078 0.024	-23.256 0.027	11.208141	0.963267	15.7313	1.00
Mel20-S8	354180784	053.770928	+50.912543	5.7358 0.0184	22.294 0.017	-25.745 0.018	11.092926	0.920669	27.2798	1.00
Mel20-S11	65697949	055.273950	+45.793793	5.2512 0.0232	20.624 0.023	-24.056 0.020	10.108564	0.800255	13.2743	1.00
Plei-S2	61146016	056.657000	+23.787720	7.4719 0.0207	20.011 0.022	-47.267 0.018	10.045166	0.900887	16.9975	1.00
Plei-S3	61145611	056.659968	+22.919778	7.1526 0.0204	19.924 0.023	-43.549 0.017	9.306278	0.657387	35.8030	1.00
Plei-S5	114029810	055.143205	+23.682609	7.4986 0.0187	20.546 0.019	-45.629 0.014	10.699779	0.911152	11.4547	1.00
Plei-S7	405484188	056.830608	+24.139115	7.2693 0.0278	19.017 0.032	-43.928 0.025	8.243902	0.353921	13.8362	1.00
Plei-S8	405483817	055.930172	+24.374568	7.4128 0.0331	19.480 0.033	-40.048 0.023	8.198288	0.348311	25.7583	...
Plei-S9	405483707	056.001121	+24.556998	7.4124 0.0278	20.535 0.032	-46.190 0.022	8.041619	0.272338	29.6633	1.00
ASCC16-S1	459991270	081.073449	+01.037743	2.9002 0.0133	1.213 0.016	-0.064 0.012	12.495133	1.089946	27.1006	0.80
ASCC16-S2	264460405	081.148573	+01.171941	2.9186 0.0129	1.320 0.013	-0.127 0.010	12.529669	1.150460	...	0.90
ASCC16-S6	459991003	081.110369	+01.446968	2.8716 0.0179	1.519 0.020	0.409 0.013	11.047515	0.803285	40.1420	1.00
ASCC16-S12	264484631	081.461492	+00.796933	2.8907 0.0153	1.408 0.016	0.156 0.012	10.606313	0.714010	39.1212	0.80
ASCC19-S1	50584002	082.061867	-01.976975	2.8229 0.0192	1.484 0.018	-1.130 0.012	10.784862	0.610453	...	0.70
ASCC19-S2	4350534	081.432092	-02.190045	2.7774 0.0245	1.172 0.018	-1.307 0.015	10.616993	0.732801	164.5130	0.80
ASCC19-S3	4289678	081.220703	-02.645501	2.8127 0.0188	1.036 0.018	-1.550 0.014	10.943126	0.675324	102.5290	0.70
ASCC19-S4	50524132	081.753548	-01.299316	2.8501 0.0186	1.118 0.018	-1.098 0.013	10.921832	0.769989	14.5996	1.00
ASCC19-S5	50619443	082.328205	-01.310307	2.7580 0.0224	0.749 0.019	-1.294 0.017	11.291587	0.792629	22.6044	0.90
ASCC19-S6	50619751	082.324391	-01.727577	2.8167 0.0237	1.190 0.021	-1.265 0.018	11.049373	0.861242	53.9130	0.90
ASCC19-S7	50524284	081.758139	-01.514830	2.9369 0.0259	1.109 0.023	-1.257 0.017	11.580762	1.096926	33.7653	0.80
ASCC19-S14	4293859	081.335941	-02.175241	2.8617 0.0374	1.418 0.031	-1.662 0.025	10.207284	0.725842	...	0.90
ASCC19-S15	50619809	082.306384	-01.796238	2.9218 0.0215	0.804 0.018	-1.278 0.015	10.297378	0.499105	53.5383	0.90
ASCC19-S16	50663177	082.577843	-02.032683	2.9615 0.0225	1.143 0.021	-1.074 0.017	10.352539	0.465540	63.8147	0.70
ASCC19-S17	50524860	081.746516	-02.360650	2.8777 0.0519	1.185 0.047	-1.122 0.035	6.579845	-0.248401	...	0.90
ASCC19-S18	50524182	081.789056	-01.367350	2.7112 0.0491	1.203 0.046	-1.549 0.032	7.186184	-0.212028	...	0.70
ASCC19-S19	50529449	081.940690	-02.145474	2.8072 0.0447	1.016 0.040	-1.199 0.029	7.488637	-0.194520	...	0.70
ASCC19-S20	4350635	081.482814	-02.335522	2.8261 0.0310	0.929 0.031	-1.551 0.022	8.263457	-0.088899	...	0.60
ASCC19-S21	50720274	082.621456	-00.847423	2.8977 0.0249	1.485 0.021	-1.190 0.019	9.292333	0.023084	28.5303	0.80
ASCC19-S22	50529597	081.910890	-01.967176	2.8701 0.0231	0.886 0.022	-1.315 0.016	9.781634	0.178481	49.0085	0.70
ASCC19-S23	50525226	081.768759	-02.921821	2.8272 0.0214	1.180 0.019	-1.523 0.015	9.787668	0.144700	130.4069	0.60
NGC2232-A2	42884139	096.948908	-04.675883	3.1433 0.0183	-4.831 0.015	-1.923 0.017	12.104153	0.860097	...	1.00
NGC2232-A3	42889061	097.140402	-04.782864	3.0053 0.0343	-4.726 0.032	-1.663 0.031	12.144907	0.868650	...	1.00
NGC2232-S3	42563198	096.615708	-04.556045	3.1514 0.0158	-4.217 0.013	-2.077 0.012	12.126466	0.794903	26.3188	1.00
NGC2232-S4	43152097	097.408543	-04.066444	2.9119 0.0152	-4.556 0.014	-1.864 0.015	11.770985	0.791048	23.8189	1.00

Notes. ^a From *Gaia* DR3 catalogue (Gaia Collaboration et al. 2023). ^b Membership probability according to Cantat-Gaudin et al. (2020).

Table A.1. continued

NGC2232-S9	42563003	096.595911	-04.656253	3.1570	0.0166	-4.746	0.015	-1.981	0.014	11.756686	0.746240	...	1.00
NGC2232-S11	43359590	097.651170	-05.376364	2.7957	0.0147	-4.900	0.015	-1.351	0.014	11.860096	0.722079	18.9535	0.50
Ros6-S1	15065608	306.468650	+38.462216	2.8976	0.0097	5.849	0.010	2.079	0.011	12.220242	0.777939	28.9528	1.00
Ros6-S2	14834047	306.454322	+38.791472	2.7869	0.0102	5.720	0.009	1.836	0.012	12.203323	0.769918	11.8291	1.00
Ros6-S5	16409631	307.558255	+38.369788	2.8279	0.0110	5.978	0.010	2.074	0.014	12.389828	0.797299	12.3145	1.00
Ros6-S9	15891271	307.184697	+40.556375	2.8307	0.0104	6.248	0.010	2.212	0.011	12.022573	0.738115	6.9740	1.00
NGC7058-S1	63706522	320.451779	+50.835362	2.7443	0.0291	7.445	0.037	2.972	0.037	9.198004	0.229628	...	0.70
NGC7058-S2	63706579	320.447802	+50.825512	2.7416	0.0141	7.424	0.018	2.399	0.016	9.662108	0.138198	...	0.80
NGC7058-S3	63854407	320.769440	+50.780969	2.7058	0.0117	7.479	0.014	2.576	0.013	11.131710	0.588780	130.1522	1.00
NGC7058-S4	63540102	320.274131	+50.821727	2.7069	0.0131	7.635	0.017	2.786	0.015	11.138639	0.608823	...	0.90
NGC7058-S5	63706944	320.313006	+50.758604	2.7254	0.0107	7.323	0.012	2.601	0.012	11.577520	0.665600	36.9123	1.00
NGC7058-S6	277385535	320.542333	+50.917663	2.7436	0.0088	7.572	0.011	2.869	0.010	12.169336	0.774905	35.6783	0.60
NGC7058-S7	63706129	320.453566	+50.910386	2.7234	0.0092	7.512	0.011	2.636	0.010	12.337247	0.819340	8.6402	0.90
NGC7058-S9	63540039	320.138783	+50.806314	2.6768	0.0197	7.615	0.023	2.762	0.022	12.635520	0.889606	...	0.80
NGC7058-S10	63706595	320.450749	+50.822663	2.7190	0.0170	7.707	0.021	2.920	0.023	12.983939	0.952257	...	0.60
NGC7058-S11	277384645	320.607971	+50.762039	2.7435	0.0101	7.612	0.012	2.764	0.012	13.135571	0.970726	...	1.00
NGC7058-S12	63706150	320.331846	+50.906027	2.7152	0.0112	7.448	0.014	3.079	0.014	13.237492	0.987474	...	0.80
NGC7058-S13	63539613	320.277208	+50.717575	2.7198	0.0106	7.411	0.012	2.883	0.013	13.291219	0.976221	...	0.90

Table A.2. Chemical abundances ($[X/H]$), relative to solar values by Grevesse et al. (2007), for stars observed in ASCC 16 (left) and Roslund 6 (right).

X	S1	S2	S6	S12	S1	S2	S5	S9
C	0.26±0.12	0.22±0.10	0.38±0.08	0.44±0.10	...	0.36±0.09
Na	-0.01±0.11	0.04±0.08	0.07±0.10	0.09±0.09	0.00±0.12	0.09±0.11	0.00±0.11	0.08±0.10
Mg	0.05±0.10	0.02±0.09	0.09±0.14	-0.03±0.13	0.05±0.09	0.00±0.11	-0.04±0.09	-0.03±0.10
Al	0.04±0.12	0.16±0.13	0.23±0.14	0.13±0.13	0.00±0.09	0.16±0.08	...	0.14±0.10
Si	-0.09±0.11	-0.04±0.12	-0.03±0.13	-0.05±0.11	-0.12±0.15	0.02±0.12	-0.15±0.13	-0.03±0.19
S	0.31±0.12	0.27±0.10	0.25±0.08	0.06±0.10	...	0.25±0.10
Ca	0.13±0.11	0.21±0.12	0.18±0.14	0.06±0.12	0.16±0.10	0.19±0.11	0.06±0.11	0.10±0.09
Sc	0.08±0.13	0.18±0.12	0.10±0.11	-0.17±0.13	0.06±0.10	0.03±0.09	-0.07±0.10	-0.11±0.12
Ti	0.12±0.13	0.24±0.11	0.19±0.12	0.02±0.14	0.02±0.12	0.05±0.08	-0.07±0.12	-0.09±0.10
V	0.10±0.11	0.22±0.11	0.13±0.12	0.15±0.13	0.15±0.11	0.15±0.12	0.07±0.11	0.08±0.11
Cr	0.08±0.12	0.19±0.12	0.14±0.14	0.02±0.14	0.14±0.11	0.15±0.10	0.03±0.12	0.06±0.12
Mn	0.14±0.11	0.21±0.12	0.08±0.13	0.04±0.13	0.16±0.13	0.11±0.12	0.07±0.12	0.05±0.13
Fe	-0.01±0.12	0.09±0.11	0.04±0.12	-0.14±0.14	-0.06±0.10	-0.03±0.11	-0.18±0.10	-0.17±0.11
Co	0.11±0.12	0.21±0.12	0.17±0.14	0.06±0.13	0.16±0.11	0.17±0.09	0.12±0.10	0.09±0.11
Ni	0.02±0.08	0.11±0.10	0.06±0.13	-0.09±0.12	-0.01±0.12	0.03±0.13	-0.16±0.13	-0.10±0.11
Cu	0.03±0.11	0.02±0.12	-0.04±0.13	-0.21±0.14	-0.06±0.09	-0.06±0.10	-0.10±0.10	...
Zn	-0.10±0.10	0.02±0.11	-0.14±0.13	-0.37±0.15	-0.29±0.11	-0.25±0.10	-0.19±0.11	...
Sr	0.14±0.10	0.18±0.09	0.21±0.12	0.03±0.12	0.08±0.09	0.07±0.10	0.11±0.09	0.14±0.11
Y	0.31±0.11	0.29±0.10	0.21±0.11	0.06±0.13	0.21±0.10	0.20±0.10	0.20±0.10	0.16±0.11
Zr	0.16±0.12	0.21±0.13	0.26±0.15	0.03±0.13	0.12±0.14	0.17±0.08	0.09±0.12	0.11±0.11
Ba	0.18±0.08	0.48±0.13	...	0.31±0.13	0.23±0.12	0.21±0.13	...	0.31±0.13
La	0.26±0.10	0.37±0.12	0.29±0.14	0.19±0.13	0.27±0.12	0.33±0.13	0.21±0.13	0.22±0.12
Ce	0.02±0.12	0.32±0.12	0.11±0.13	0.13±0.14	0.04±0.09	0.14±0.08	0.16±0.10	0.13±0.09
Pr	0.13±0.10	...	0.21±0.12	0.13±0.12
Nd	0.21±0.11	0.24±0.12	0.19±0.13	0.18±0.14	0.29±0.12	0.29±0.11	0.14±0.12	0.19±0.11

Table A.3. Chemical abundances ($[X/H]$), relative to solar values by Grevesse et al. (2007), for stars observed in Melotte 20.

X	S1	S2	S3	S8	A1*	A2	A3
C	0.40±0.18	0.16±0.12
Na	0.08±0.08	0.02±0.17	0.03±0.14	0.04±0.12	0.33±0.14	-0.11±0.17	-0.15±0.12
Mg	0.01±0.11	-0.01±0.12	-0.05±0.13	-0.04±0.13	-0.02±0.12	-0.07±0.14	-0.18±0.16
Al	0.02±0.13	0.14±0.12	0.33±0.16	0.13±0.13	0.45±0.12	-0.07±0.12	0.25±0.13
Si	-0.16±0.13	-0.19±0.15	-0.15±0.14	-0.11±0.13	-0.06±0.10	-0.16±0.14	-0.10±0.14
S	0.37±0.12	0.09±0.10
Ca	0.16±0.11	0.17±0.12	0.16±0.09	0.13±0.11	-0.03±0.13	0.02±0.12	-0.14±0.16
Sc	-0.06±0.11	-0.05±0.12	-0.07±0.09	-0.10±0.12	0.06±0.14	-0.09±0.12	-0.12±0.13
Ti	0.03±0.13	0.04±0.12	0.05±0.12	-0.01±0.11	-0.13±0.13	-0.13±0.12	-0.21±0.16
V	0.14±0.11	0.16±0.11	0.15±0.14	0.12±0.10	0.06±0.11	0.04±0.14	-0.01±0.13
Cr	0.06±0.12	0.11±0.11	0.12±0.12	0.11±0.13	0.02±0.13	-0.04±0.14	-0.12±0.16
Mn	0.14±0.12	0.13±0.12	0.14±0.13	0.11±0.12	0.09±0.13	0.07±0.13	-0.10±0.15
Fe	-0.04±0.11	-0.02±0.12	-0.03±0.10	-0.07±0.12	-0.31±0.14	-0.20±0.13	-0.36±0.15
Co	0.08±0.10	0.09±0.10	0.14±0.11	0.08±0.11	0.11±0.12	0.07±0.12	-0.04±0.11
Ni	-0.08±0.12	-0.05±0.09	-0.04±0.11	-0.07±0.10	-0.07±0.13	-0.11±0.11	-0.24±0.15
Cu	0.03±0.10	-0.03±0.08	-0.07±0.09	-0.03±0.10	0.03±0.10	-0.22±0.12	-0.12±0.13
Zn	-0.24±0.08	-0.21±0.10	-0.22±0.11	-0.22±0.09	-0.20±0.15	-0.25±0.12	-0.50±0.14
Sr	0.16±0.12	0.12±0.07	0.09±0.08	0.17±0.12	0.23±0.15	0.24±0.07	0.30±0.12
Y	0.22±0.13	0.25±0.11	0.24±0.13	0.21±0.10	0.12±0.13	0.16±0.16	0.07±0.14
Zr	0.11±0.12	0.08±0.11	0.16±0.13	0.17±0.14	0.04±0.13	0.06±0.14	0.02±0.12
Mo	0.19±0.18	0.25±0.17	0.25±0.14
Ba	0.40±0.13	0.22±0.12	0.50±0.18	0.35±0.13	-0.21±0.17	0.40±0.10	-0.06±0.15
La	0.24±0.12	0.27±0.13	0.28±0.12	0.20±0.14	0.21±0.13	0.25±0.14	0.14±0.12
Ce	0.12±0.09	0.09±0.09	0.03±0.12	0.10±0.11	0.11±0.12	0.02±0.12	0.11±0.09
Pr	...	0.13±0.12	0.08±0.14	0.17±0.12
Nd	0.28±0.12	0.27±0.13	0.21±0.12	0.24±0.13	0.14±0.12	0.16±0.15	0.09±0.14

Note. * Non member.

Table A.4. Chemical abundances ($[X/H]$), relative to solar values by Grevesse et al. (2007), for stars observed in NGC 2232 (left) and Pleiades (right).

X	S3	S9	S11	A2	A3	S3	S5
C	0.38±0.06	0.21±0.12	...
Na	0.09±0.09	0.02±0.11	-0.06±0.13	0.07±0.12	-0.03±0.12	0.02±0.14	0.12±0.12
Mg	-0.02±0.14	-0.01±0.09	-0.01±0.15	0.01±0.13	-0.03±0.07	0.01±0.12	0.10±0.11
Al	0.16±0.15	0.01±0.12	0.07±0.10	0.18±0.17	0.07±0.18	0.08±0.12	0.20±0.09
Si	-0.06±0.14	-0.09±0.12	-0.06±0.15	-0.11±0.11	-0.16±0.16	0.00±0.14	-0.13±0.12
S	0.29±0.12	0.18±0.13	0.31±0.11
Ca	0.19±0.12	0.10±0.13	0.06±0.15	0.18±0.14	0.11±0.17	0.02±0.09	0.16±0.12
Sc	0.05±0.12	0.03±0.13	0.02±0.17	0.02±0.14	-0.01±0.16	-0.08±0.13	0.07±0.12
Ti	0.06±0.12	-0.03±0.13	-0.06±0.14	0.12±0.12	-0.06±0.13	-0.06±0.13	0.16±0.12
V	0.22±0.11	0.12±0.12	0.17±0.09	0.22±0.10	0.12±0.14	0.19±0.14	0.17±0.12
Cr	0.12±0.11	0.03±0.13	0.00±0.14	0.11±0.13	0.04±0.13	0.01±0.13	0.19±0.09
Mn	0.14±0.09	0.07±0.15	0.11±0.13	0.14±0.11	0.08±0.09	0.00±0.08	0.23±0.10
Fe	-0.01±0.10	-0.18±0.11	-0.21±0.14	0.00±0.11	-0.15±0.12	-0.17±0.13	0.12±0.09
Co	0.14±0.09	0.07±0.10	0.09±0.11	0.14±0.10	0.05±0.10	0.13±0.12	0.22±0.13
Ni	0.03±0.12	-0.11±0.13	-0.13±0.13	-0.01±0.10	-0.15±0.13	-0.04±0.12	0.08±0.06
Cu	-0.09±0.12	0.07±0.14	-0.24±0.17	0.00±0.14	0.12±0.15	-0.26±0.18	0.12±0.15
Zn	-0.24±0.07	-0.27±0.06	-0.37±0.07	-0.17±0.10	-0.27±0.13	-0.43±0.14	-0.15±0.12
Sr	0.10±0.06	0.06±0.08	0.14±0.17	0.03±0.06	0.02±0.14	0.00±0.15	0.15±0.12
Y	0.22±0.15	0.24±0.16	0.10±0.17	0.28±0.13	0.20±0.14	0.11±0.11	0.29±0.13
Zr	0.16±0.06	0.16±0.13	0.10±0.16	0.18±0.10	0.13±0.09	0.15±0.12	0.27±0.11
Ba	0.50±0.06	0.46±0.09	0.35±0.14	0.49±0.10	0.45±0.08	0.24±0.13	0.30±0.12
La	0.26±0.10	0.19±0.11	0.27±0.17	0.30±0.15	0.25±0.15	0.31±0.10	0.26±0.07
Ce	0.23±0.14	0.07±0.13	0.09±0.13	0.21±0.13	0.15±0.13	0.19±0.14	0.16±0.12
Pr	0.21±0.13	0.15±0.07	...	0.21±0.12	0.29±0.12	0.15±0.14	0.20±0.13
Nd	0.30±0.13	0.16±0.11	0.20±0.15	0.18±0.12	0.18±0.12	0.21±0.13	0.28±0.11

Table A.5. Chemical abundances ($[X/H]$), relative to solar values by Grevesse et al. (2007), for stars observed in ASCC 19.

X	S1	S2	S3	S4	S5	S6	S14	S15	S16
C	0.11±0.14	0.25±0.15	0.20±0.16	...	0.16±0.12	...	0.24±0.12	0.13±0.13	0.16±0.11
Na	0.23±0.15	-0.13±0.17	0.08±0.16	0.20±0.12	0.00±0.13	0.17±0.09	-0.06±0.14	-0.28±0.16	0.16±0.13
Mg	0.02±0.11	-0.05±0.12	-0.05±0.13	0.08±0.09	-0.01±0.09	0.02±0.10	-0.12±0.08	-0.06±0.12	-0.20±0.09
Al	0.10±0.12	0.20±0.13	0.18±0.13	...	0.19±0.12
Si	0.06±0.10	-0.09±0.13	-0.07±0.12	0.05±0.11	-0.14±0.09	-0.01±0.09	-0.12±0.09	-0.13±0.11	0.05±0.10
S	0.21±0.13	0.19±0.11	0.25±0.11	0.20±0.12	0.18±0.12	0.27±0.23
Ca	0.06±0.12	0.05±0.14	0.06±0.15	0.16±0.11	0.08±0.10	0.16±0.10	0.04±0.10	0.10±0.11	0.01±0.08
Sc	-0.08±0.11	-0.13±0.14	-0.13±0.13	0.03±0.08	-0.11±0.10	0.00±0.09	-0.10±0.09	-0.11±0.12	-0.15±0.10
Ti	0.01±0.12	-0.04±0.14	-0.02±0.13	0.18±0.11	-0.04±0.11	0.07±0.10	-0.01±0.11	0.03±0.13	-0.06±0.12
V	0.23±0.12	0.12±0.14	0.00±0.14	0.27±0.12	0.10±0.11	0.34±0.11	0.15±0.10	0.14±0.12	0.10±0.11
Cr	0.03±0.12	-0.12±0.15	-0.01±0.13	0.25±0.12	-0.02±0.08	0.21±0.11	0.03±0.09	-0.05±0.12	-0.06±0.10
Mn	-0.09±0.13	-0.08±0.13	-0.05±0.12	0.12±0.09	-0.07±0.11	0.06±0.10	-0.04±0.10	-0.06±0.12	0.00±0.09
Fe	-0.17±0.13	-0.29±0.15	-0.22±0.14	0.15±0.12	-0.22±0.11	0.06±0.10	-0.23±0.10	-0.20±0.13	-0.24±0.11
Co	0.15±0.12	0.12±0.15	0.22±0.16	0.26±0.13	0.10±0.12	0.23±0.12	0.20±0.12	0.15±0.13	0.22±0.11
Ni	-0.05±0.12	-0.09±0.14	0.02±0.13	0.11±0.09	-0.11±0.09	0.00±0.10	-0.09±0.10	-0.12±0.12	-0.18±0.10
Cu	0.00±0.13	-0.13±0.14	-0.13±0.15	-0.03±0.12	-0.22±0.11	-0.04±0.11	-0.35±0.12	...	-0.06±0.11
Zn	-0.19±0.16	-0.19±0.12	-0.39±0.13	-0.18±0.12	-0.39±0.13	...	-0.31±0.12
Sr	0.05±0.12	-0.02±0.10	0.32±0.12	0.19±0.08	0.18±0.11	0.02±0.09
Y	-0.04±0.12	-0.14±0.14	0.04±0.14	0.30±0.13	0.15±0.11	0.23±0.12	0.12±0.09	-0.02±0.12	-0.01±0.10
Zr	0.15±0.13	...	0.12±0.14	...	0.17±0.13	0.11±0.11	0.19±0.11	0.22±0.13	0.18±0.13
Ba	0.27±0.13	0.21±0.15	0.27±0.16	0.17±0.11	0.34±0.12	0.39±0.15	0.18±0.09
La	0.21±0.11	...	0.16±0.13	...	0.23±0.09	0.20±0.09	0.27±0.10	0.25±0.10	0.20±0.09
Ce	0.21±0.13	0.16±0.15	0.10±0.11	0.26±0.12	0.17±0.11	0.20±0.12	0.14±0.12
Pr	0.20±0.11	0.21±0.12	0.22±0.11
Nd	0.19±0.14	0.19±0.16	0.16±0.08	...	0.13±0.12	0.19±0.12	0.18±0.13	...	0.11±0.12

Table A.6. Chemical abundances ($[X/H]$), relative to solar values by Grevesse et al. (2007), for stars observed in NGC 7058.

X	S3	S4	S5	S6	S7
C	-0.07±0.14	0.13±0.13	0.10±0.11	0.32±0.10	...
Na	0.15±0.13	0.16±0.14	0.16±0.11	0.14±0.10	0.24±0.10
Mg	-0.02±0.13	0.00±0.12	0.02±0.11	0.07±0.09	0.14±0.10
Al	0.10±0.10	...	0.10±0.12
Si	-0.06±0.15	-0.06±0.13	-0.09±0.13	-0.08±0.12	-0.14±0.11
S	0.19±0.12	0.28±0.12	0.31±0.10	...	0.19±0.10
Ca	0.04±0.13	0.00±0.14	-0.09±0.11	0.10±0.10	0.24±0.10
Sc	-0.11±0.12	-0.12±0.13	-0.20±0.11	-0.11±0.10	0.03±0.12
Ti	-0.04±0.15	-0.01±0.14	0.01±0.12	0.01±0.11	0.11±0.12
V	0.10±0.14	0.00±0.13	0.12±0.12	0.08±0.11	0.16±0.10
Cr	-0.03±0.13	-0.03±0.14	-0.06±0.11	0.03±0.11	0.15±0.12
Mn	0.02±0.13	0.00±0.13	-0.06±0.11	0.10±0.12	0.13±0.12
Fe	-0.12±0.14	-0.11±0.15	-0.15±0.13	-0.06±0.12	0.00±0.09
Co	0.21±0.13	0.25±0.13	0.15±0.11	0.16±0.12	0.14±0.11
Ni	0.02±0.14	-0.01±0.13	-0.02±0.10	-0.01±0.10	0.09±0.11
Cu	-0.19±0.12	-0.06±0.09	-0.07±0.10
Zn	...	-0.25±0.15	-0.31±0.14	-0.07±0.12	-0.07±0.11
Sr	...	0.05±0.15	0.06±0.12	0.35±0.13	0.10±0.12
Y	0.01±0.13	0.11±0.13	0.00±0.09	0.09±0.10	0.23±0.11
Zr	0.16±0.13	0.14±0.13	0.17±0.11	0.12±0.12	0.07±0.10
Ba	0.23±0.14	...	0.37±0.13	0.35±0.13	...
La	0.06±0.14	0.11±0.13	0.25±0.12	0.36±0.10	0.33±0.12
Ce	0.06±0.14	0.02±0.14	0.13±0.12	0.04±0.19	0.13±0.12
Pr	0.13±0.13	0.13±0.14
Nd	0.18±0.13	0.15±0.14	0.17±0.12	0.27±0.12	0.31±0.11

X	S9	S10	S11	S12	S13
C
Na	0.15±0.09	0.20±0.08	0.19±0.11	0.16±0.10	0.11±0.09
Mg	0.07±0.10	0.08±0.11	0.17±0.10	0.17±0.09	0.01±0.08
Al	0.12±0.12	0.18±0.12	0.20±0.13	...	0.14±0.09
Si	-0.10±0.12	-0.12±0.12	-0.08±0.12	-0.16±0.11	-0.11±0.13
S
Ca	0.08±0.09	0.21±0.11	0.33±0.12	0.16±0.11	0.07±0.10
Sc	0.00±0.11	0.04±0.11	0.08±0.11	0.06±0.12	-0.05±0.12
Ti	0.04±0.10	0.13±0.12	0.19±0.12	0.14±0.11	-0.10±0.12
V	0.10±0.12	0.16±0.09	0.30±0.10	0.18±0.08	0.03±0.11
Cr	0.04±0.10	0.16±0.12	0.27±0.12	0.19±0.12	-0.01±0.12
Mn	0.12±0.11	0.13±0.10	0.22±0.12	0.20±0.11	0.00±0.10
Fe	-0.06±0.10	0.02±0.09	0.19±0.12	0.07±0.12	-0.11±0.13
Co	0.14±0.12	0.17±0.09	0.23±0.11	0.06±0.10	0.02±0.11
Ni	0.03±0.11	0.04±0.12	0.09±0.09	0.05±0.10	-0.06±0.11
Cu	-0.04±0.10	-0.02±0.10	0.14±0.11	0.06±0.11	...
Zn	-0.19±0.12	-0.13±0.12	-0.22±0.12	-0.15±0.11	...
Sr	...	0.05±0.12	0.19±0.13	...	0.30±0.13
Y	0.16±0.09	0.10±0.09	0.21±0.12	0.14±0.11	0.15±0.14
Zr	0.17±0.11	0.10±0.10	0.23±0.12	0.16±0.11	0.02±0.12
Ba	0.26±0.11	0.27±0.12	0.33±0.11
La	0.23±0.12	...	0.26±0.11
Ce	...	0.27±0.10	0.24±0.12
Pr	0.38±0.11
Nd	...	0.24±0.12	0.30±0.11	0.30±0.12	0.27±0.12

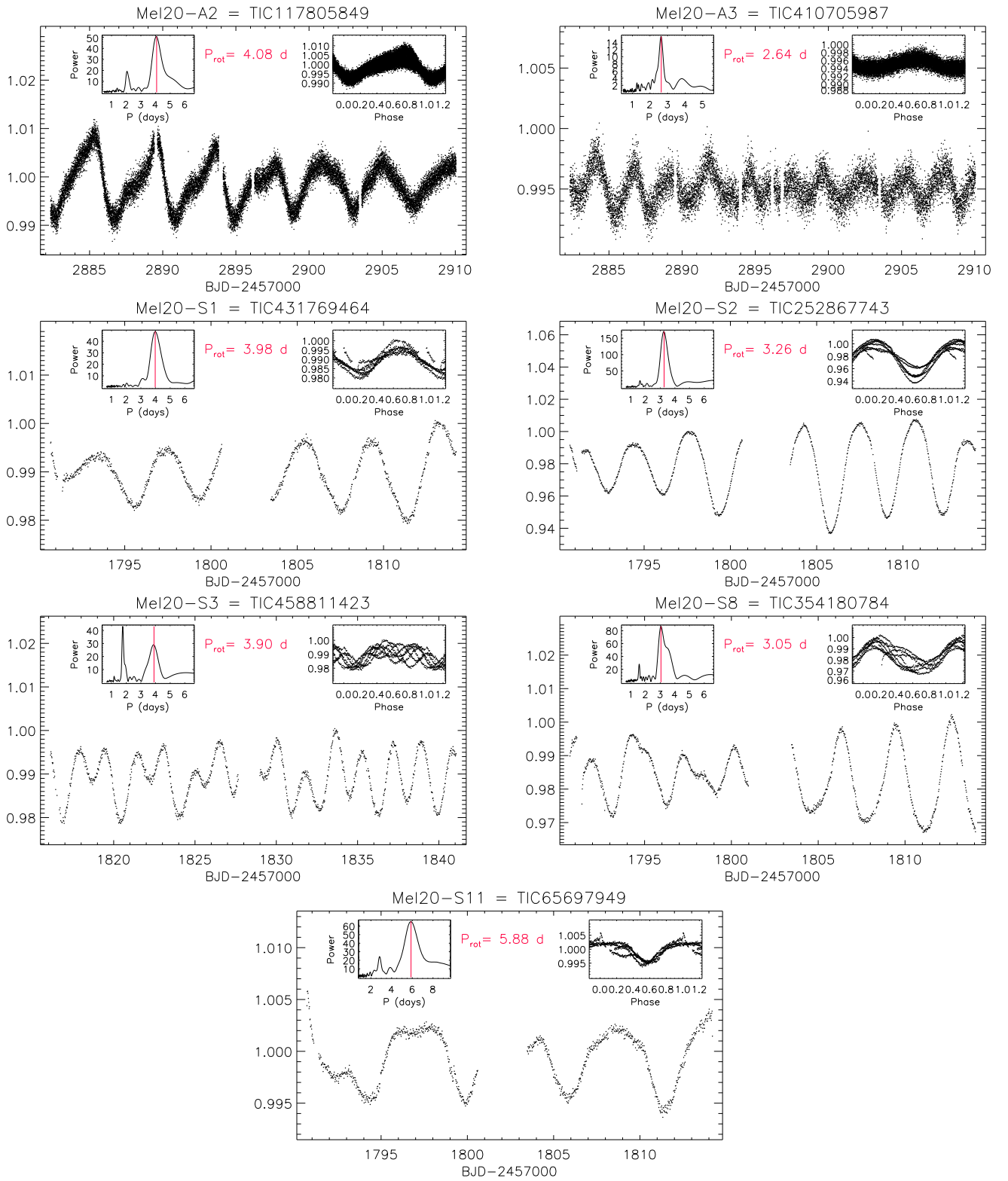


Fig. A.1. *TESS* light curves for the four members of Melotte 20. In each panel, the inset in the upper left corner shows the cleaned periodogram, with the period marked by a vertical red line and indicated with red characters. The inset in the upper right corner displays the data phased with this period.

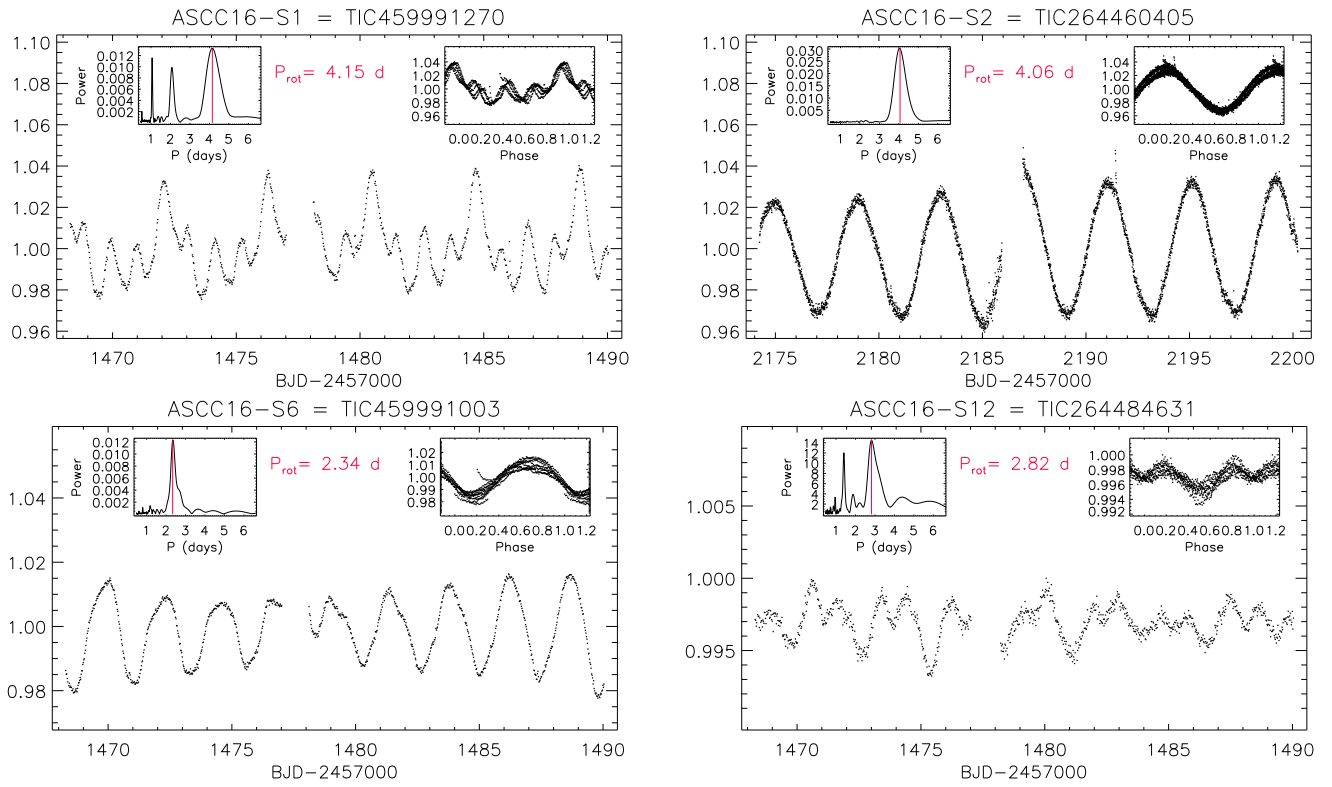


Fig. A.2. TESS light curves for the four members of ASCC 16. In each panel, the inset in the upper left corner shows the cleaned periodogram, with the period marked by a vertical red line and indicated with red characters. The inset in the upper right corner displays the data phased with this period.

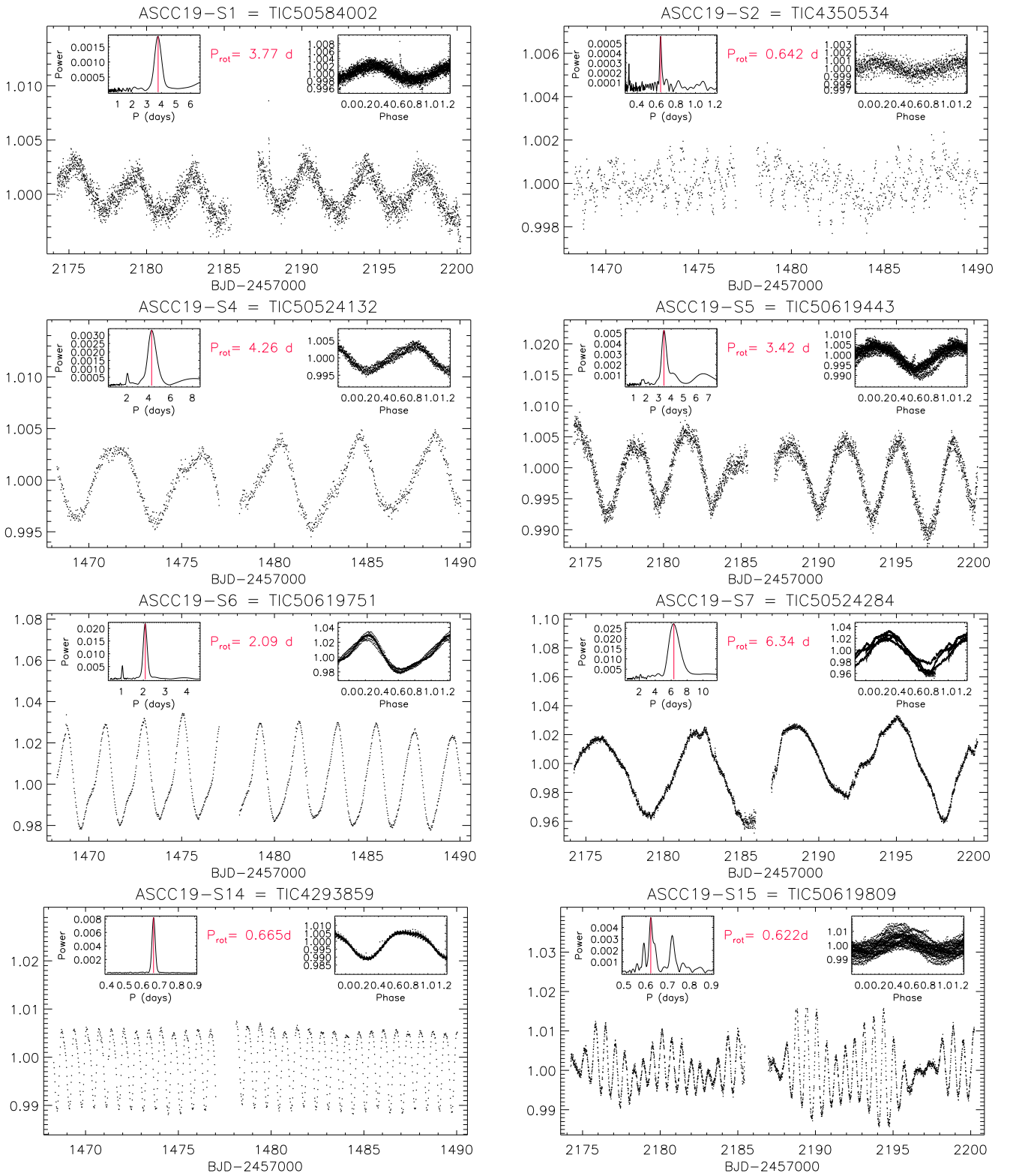


Fig. A.3. *TESS* light curves for eight members of ASCC 19. In each panel, the inset in the upper left corner shows the cleaned periodogram, with the period marked by a vertical red line and indicated with red characters. The inset in the upper right corner displays the data phased with this period.

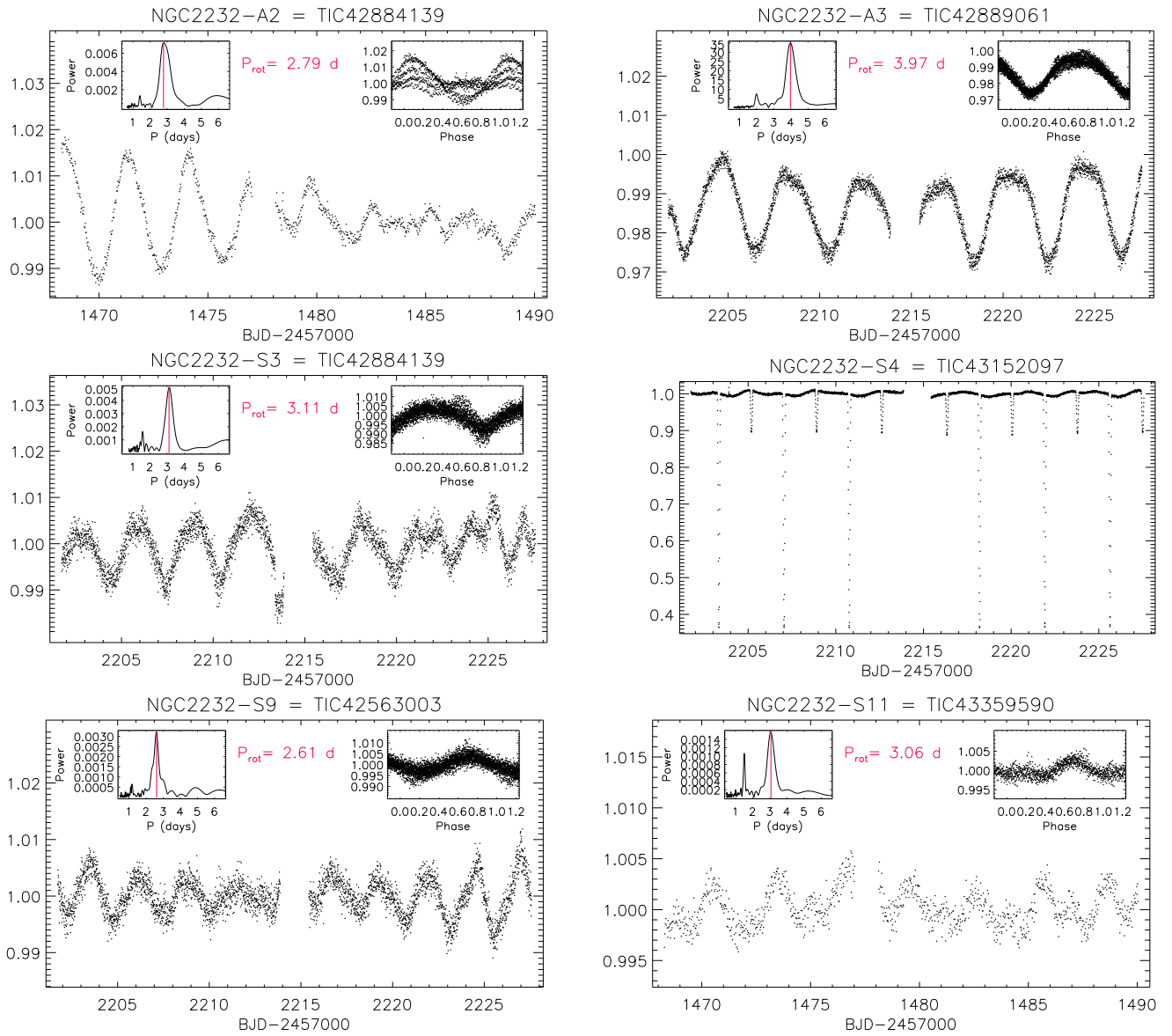


Fig. A.4. *TESS* light curves for six members of NGC 2232. In each panel, the inset in the upper left corner shows the cleaned periodogram, with the period marked by a vertical red line and indicated with red characters. The inset in the upper right corner displays the data phased with this period.

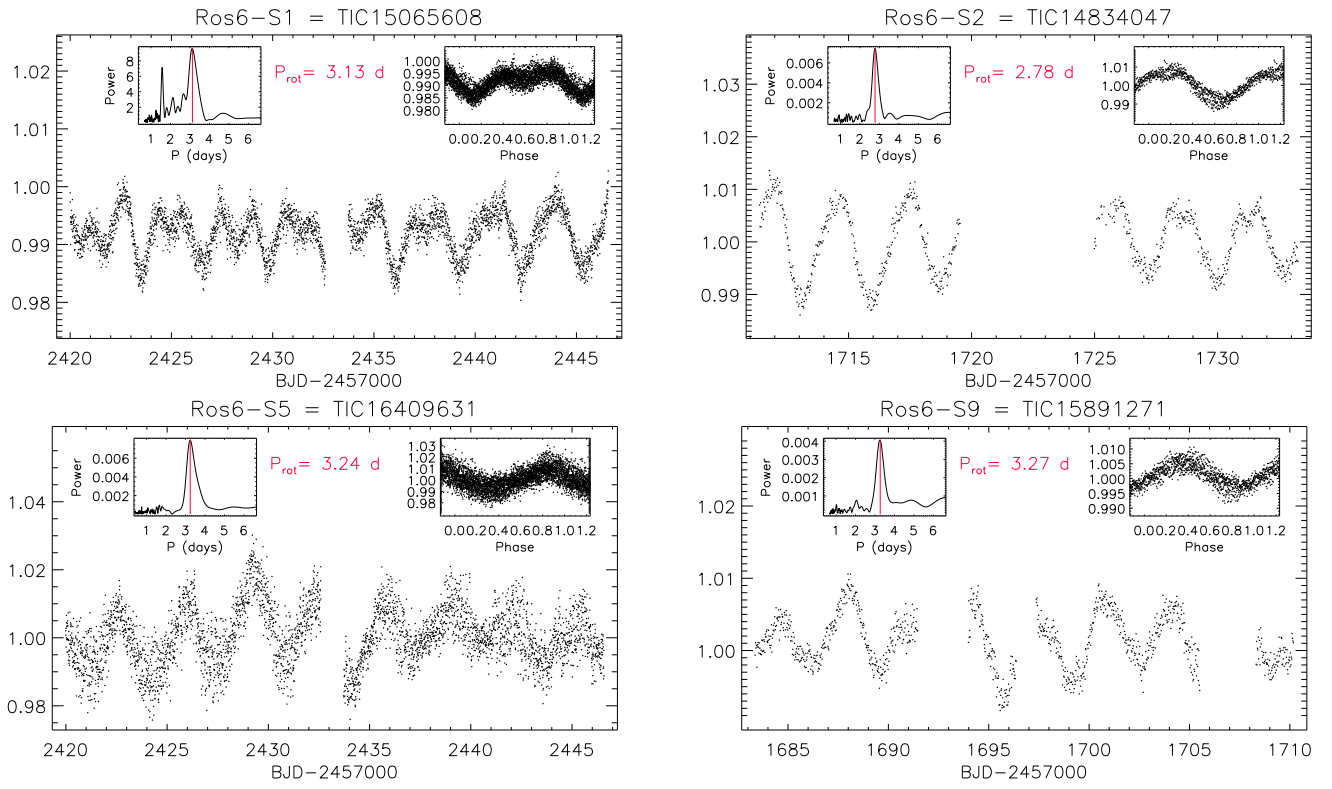


Fig. A.5. *TESS* light curves for the four members of Roslund 6. In each panel, the inset in the upper left corner shows the cleaned periodogram, with the period marked by a vertical red line and indicated with red characters. The inset in the upper right corner displays the data phased with this period.

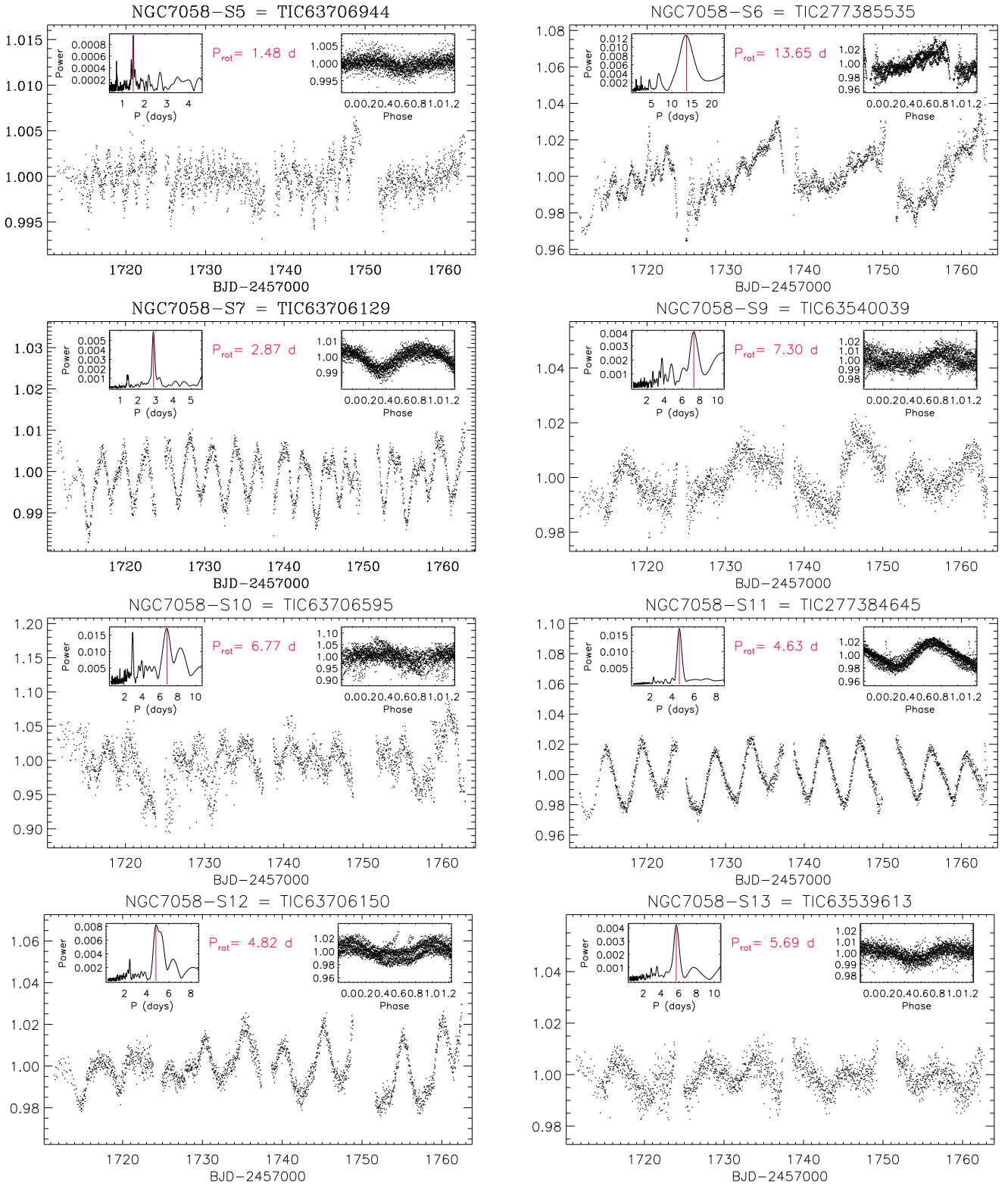


Fig. A.6. *TESS* light curves for eight members of NGC 7058. In each panel, the inset in the upper left corner shows the cleaned periodogram, with the period marked by a vertical red line and indicated with red characters. The inset in the upper right corner displays the data phased with this period.

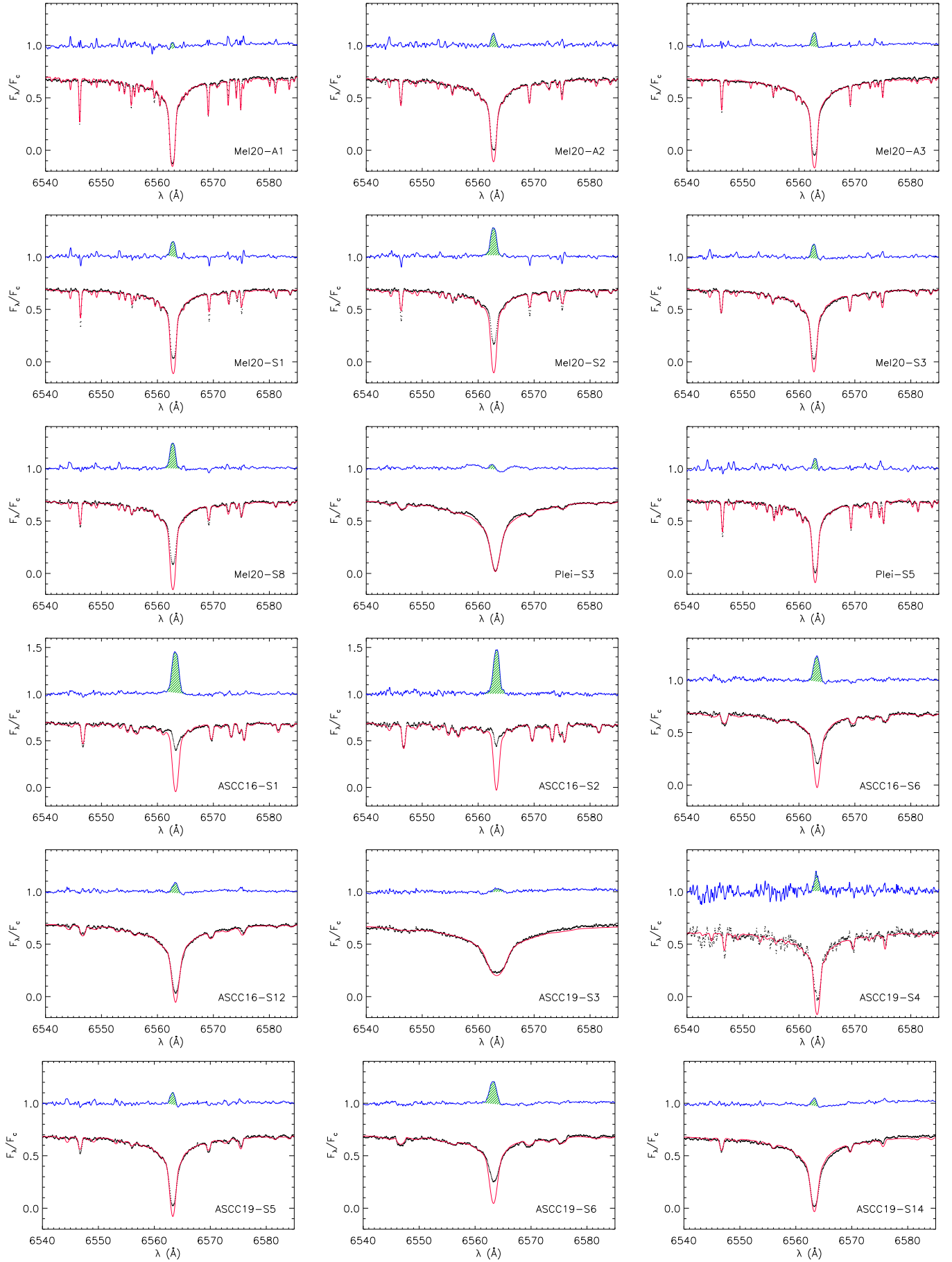


Fig. A.7. HARPS-N spectra of the investigated stars in the H α region. In each box, the non-active template (red line) is overlaid with the observed spectrum (black dots). The chromospheric emission which fills in the H α core is clearly visible in the subtracted spectrum (blue line in each panel). The green hatched area represents the excess H α emission that was integrated to obtain $W_{H\alpha}$. The ID of the source is marked in the lower right corner of each box.

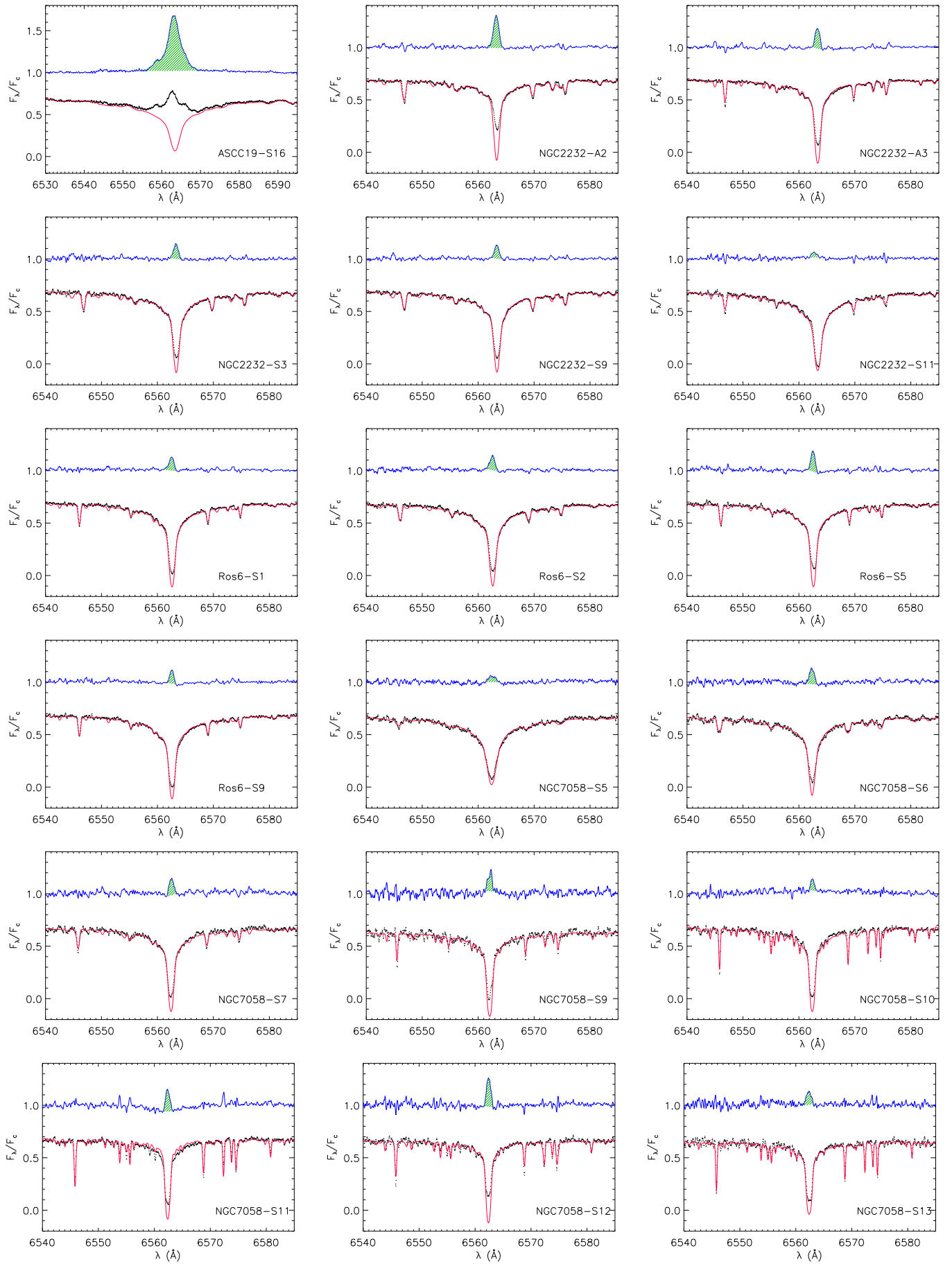


Fig. A.7. *Continued*

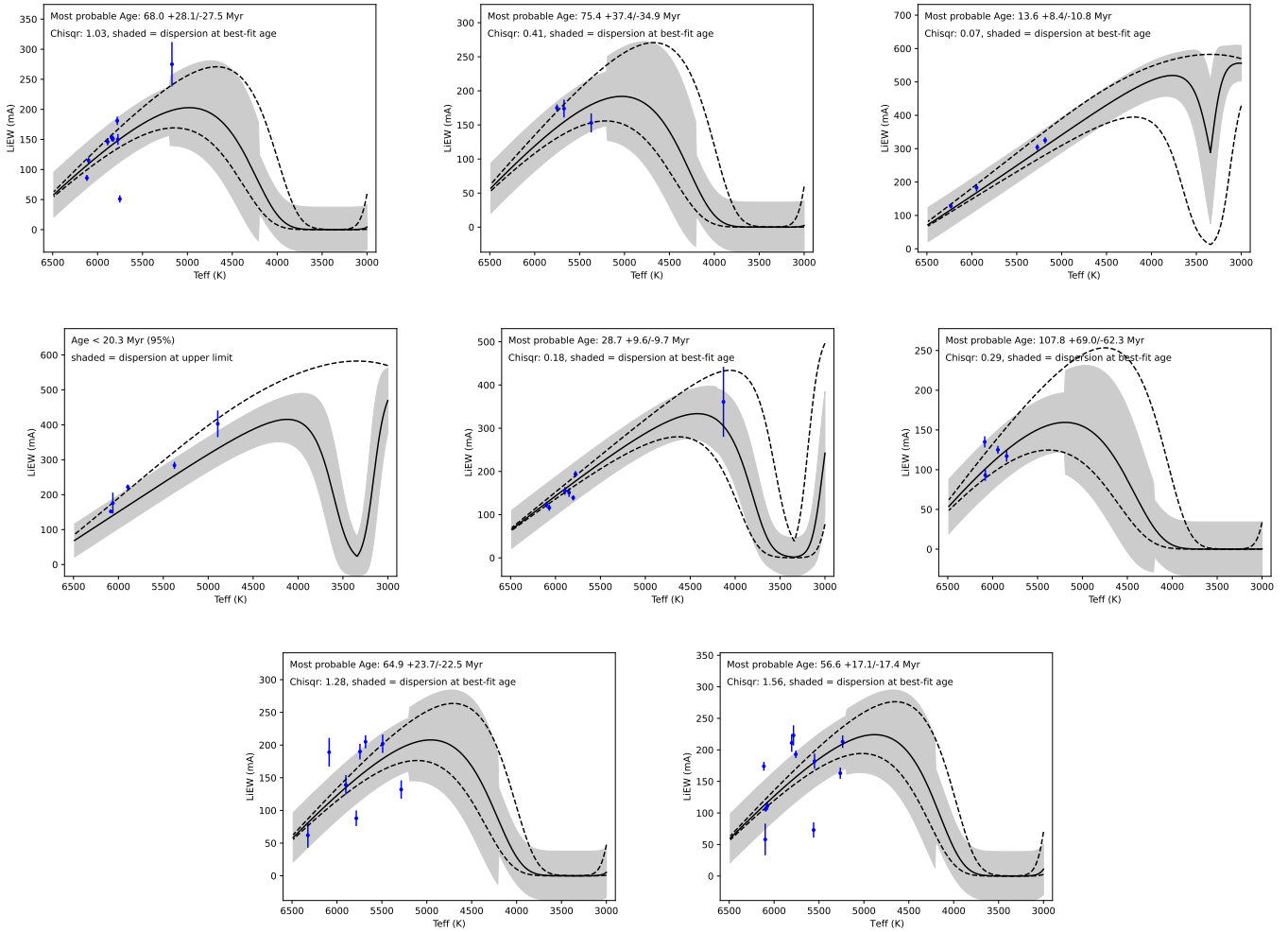


Fig. A.8. Fit to the lithium depletion pattern of the members of the investigated clusters made with the EAGLES code (Jeffries et al. 2023).

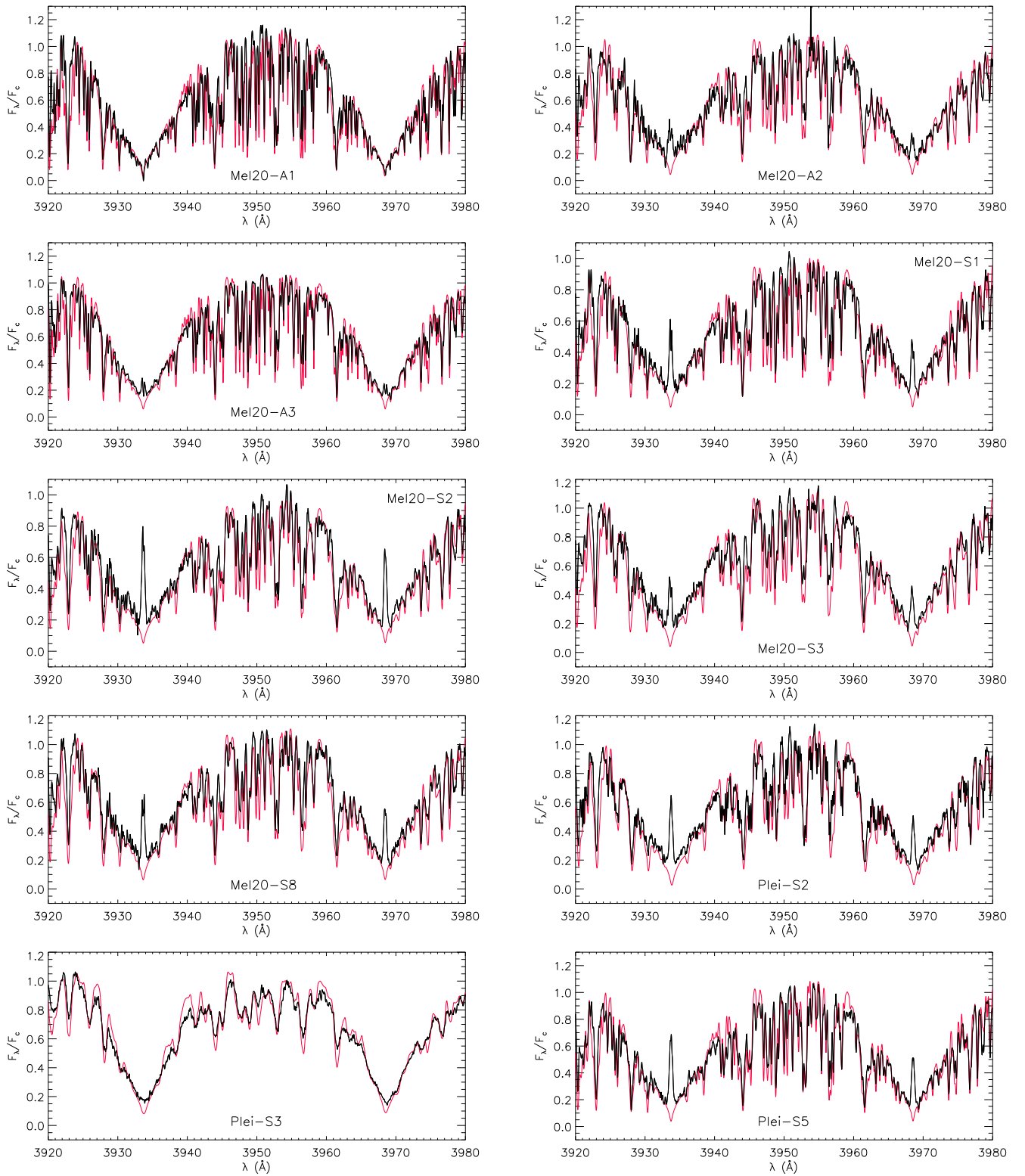


Fig. A.9. HARPS-N spectra of the investigated stars in the Ca II H&K region. In each box, the non-active template (red line) is overlaid with the observed spectrum (black dots). The ID of the source is marked in the lower right corner of each box.

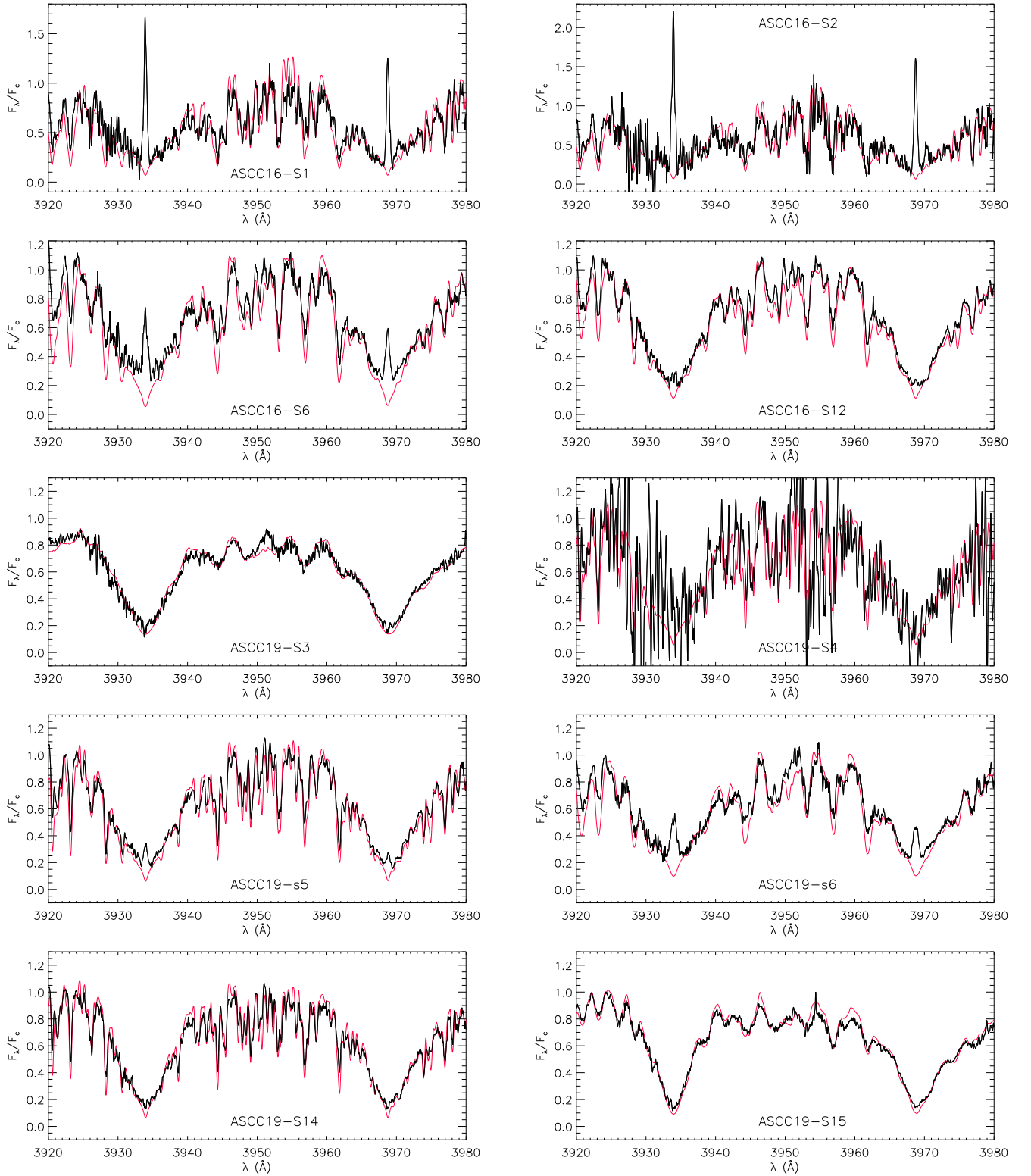
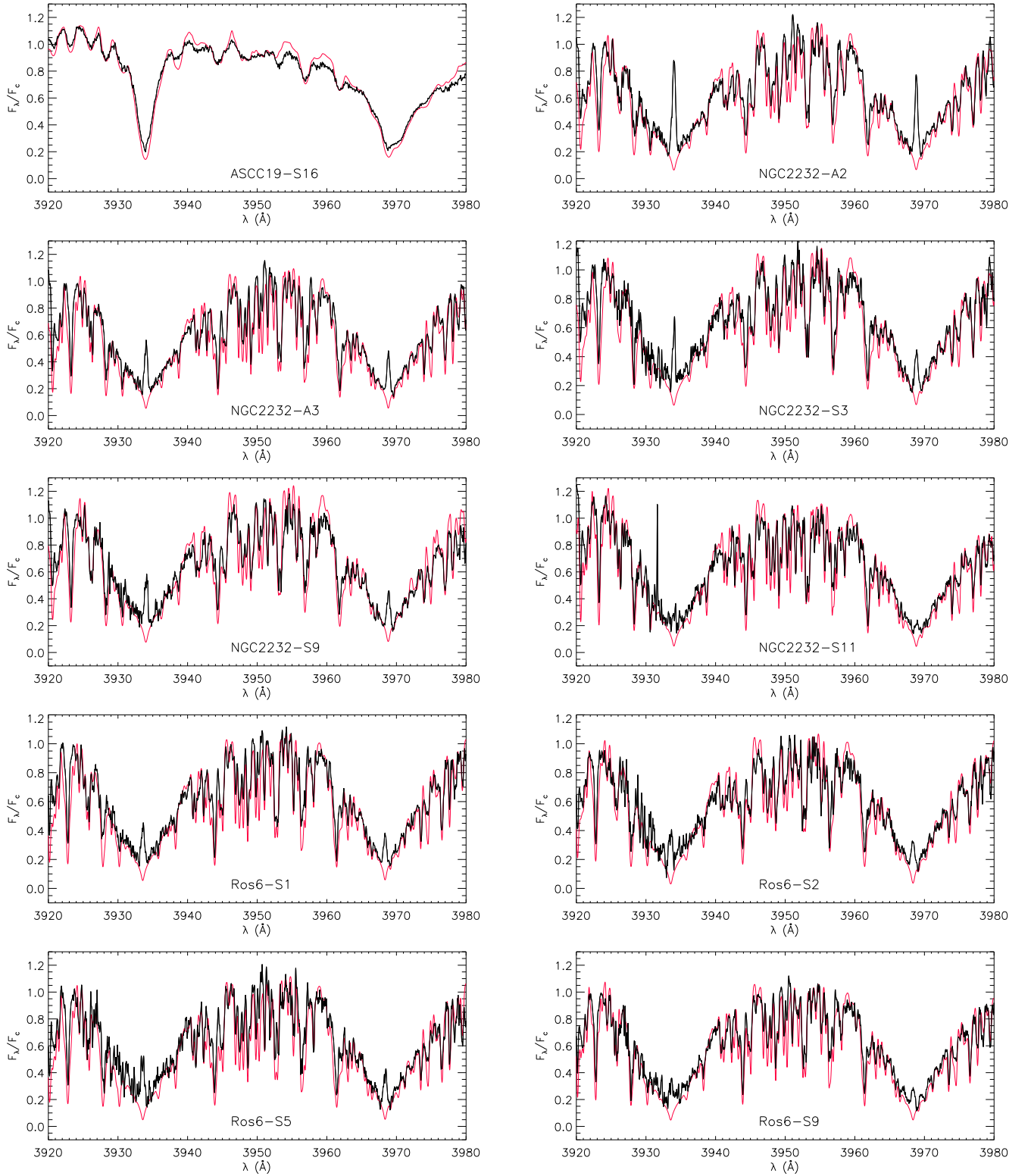


Fig. A.9. *Continued*

Fig. A.9. *Continued*

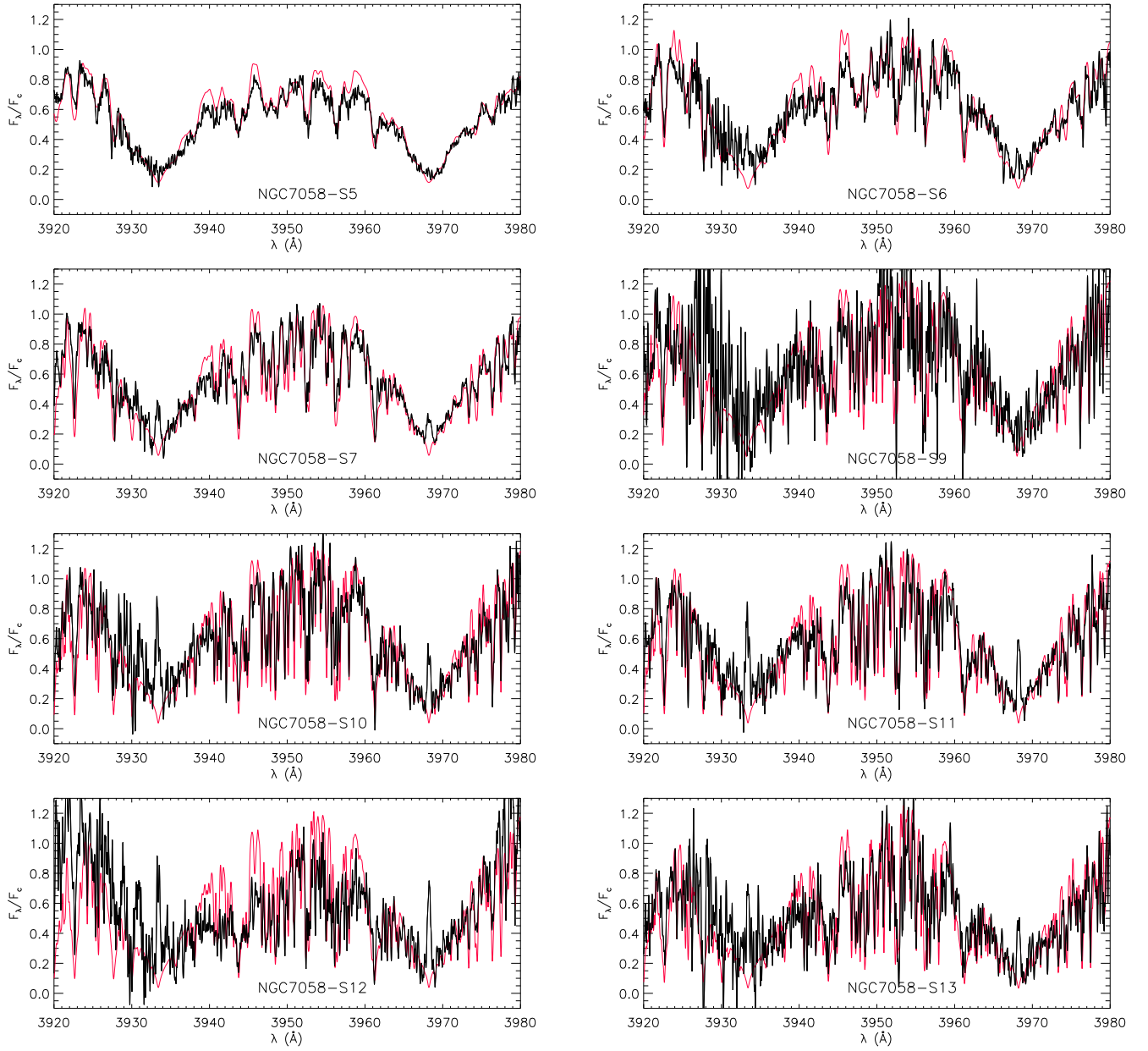


Fig. A.9. *Continued*